Correlation of Structure and Magnetic Properties in Charge-transfer Salt Molecular Magnets Composed of Decamethylmetallocene Electron Donors and Organic Electron Acceptors

William Stuart Tyree

Thesis submitted to the faculty of the Virginia Polytechnic Institute and State University in partial fulfillment of the requirements for the degree of

Master of Science
In
Chemistry

Gordon Yee, Committee Chair
Brian Hanson, Committee Member
Karen Brewer, Committee Member

August 2, 2005
Blacksburg, Virginia

Keywords: charge-transfer salt magnets, metallocene-based magnets, molecular magnetism, through-space coupling

Correlation of Structure and Magnetic Properties in Charge-transfer Salt Molecular Magnets Composed of Decamethylmetallocene Electron Donors and Organic Electron Acceptors

William Stuart Tyree

ABSTRACT

Di-*n*-propyl dicyanofumarate (D*n*PrDCF) and di-isopropyl dicyanofumarate (D*i*PrDCF) have been used as one-electron acceptors in the synthesis of charge-transfer salt magnets with decamethylmetallocenes, MCp^*_2 (M = Mn, Cr). Salts of each acceptor with each metallocene have been characterized and the structures of the chromium analogues have been solved. The two acceptors are structurally similar to dimethyl dicyanofumarate (DMeDCF) and diethyl dicyanofumarate (DEtDCF), which have been previously studied and found to form charge-transfer salt magnets with the aforementioned decamethylmetallocenes. A typical structural motif is present in these types of charge-transfer salts which allows for the comparison of magnetic properties based on the length or size of the alkyl group of the dialkyl dicyanofumarate. Some trends were established based on the magnetic properties of the homologous series including ordering temperature/bulkiness of the alkyl group and intrastack distances/θ values. Correlation of magnetic and structural properties may give some insight into "through-space" magnetic coupling, of which little is understood.

Table of Contents

List of Figures

List of Tables

Chapter I: General Magnetism

It has been proposed that mankind has known about magnetism for well over two thousand years. There is a story of the shepherd, Magnus, who discovered the naturally occurring magnet lodestone in a land later named Magnesia in Asia Minor around 900 B.C. Supposedly the lodestone pulled the nails out of his sandals and the metal tip off his walking stick while he was walking over it. More commonly, the Greek philosopher Thales of Miletus is credited with the discovery of magnetism in lodestone around 600 B.C. The Chinese used the magnetic properties of lodestone to develop the compass, but little was known about magnetism until the 1800's. Lodestone, which is essentially magnetite (Fe_3O_4) of a particular composition and crystal structure that has been exposed to a strong magnetic field, was the only known magnet until the mid 1800's with the advent of magnetized carbon steel.

William Gilbert published the first systematic experiments on magnetism in 1600 with *De Magnete*. However, the history of magnetism as a scientific topic did not take off until the 1800's with the discovery of the connection of electricity and magnetism by Oersted. Between then and the 20^{th} century, a considerable amount of general research took place that afforded many important discoveries; a few of these included the development of methods for measuring magnetic susceptibilities by Faraday and Gouy, a system for predicting diamagnetic susceptibilities by P. Pascal, and studies on the temperature dependence of paramagnetism by Pierre Curie. By the turn of the century, the experimental groundwork had been laid for fundamental theories such as the Curie Law as well as a general understanding of diamagnetism, paramagnetism, and ferromagnetism.

1. Magnetic Susceptibility

The magnetic susceptibility (χ) of a material is the quantitative measure of the response of a material to an externally applied magnetic field. It can be defined by the following equation:

$$\chi = \frac{M}{H} \qquad (1)$$

The magnetization of the material (M) has units of emu·G/mol, the externally applied magnetic field (H) has units of Gauss (G), and the molar magnetic susceptibility (χ) has units of emu/mol. The magnetization refers to the amount of individual magnetic moments within the material that are aligned with the applied field. Materials that are slightly repelled by the field are referred to as diamagnetic. Other materials that are attracted to the field are called paramagnetic.

Diamagnetism is a property of all compounds that arises with the interaction of paired electrons with an applied magnetic field. These compounds are weakly repelled by the applied field due to the orbital motion of electrons induced by the external field which creates an opposing magnetic field. When these materials are subjected to a magnetic field, they reduce the density of the field lines around them or, in the case of a non-

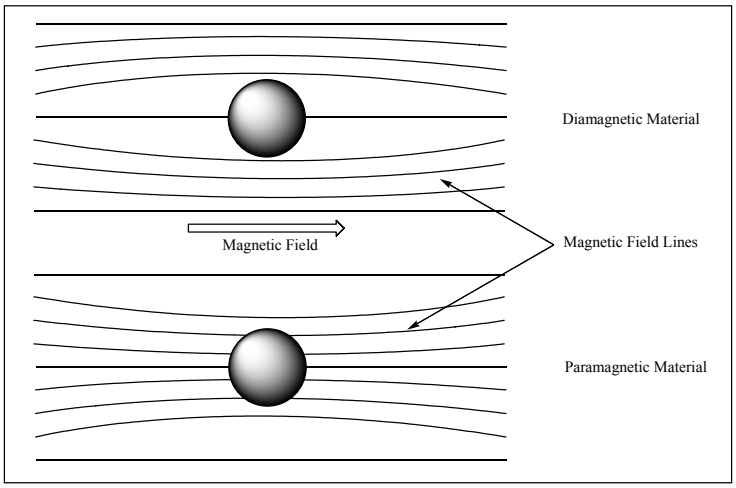

Figure 1.1 This illustration is symbolic of how diamagnetic and paramagnetic materials interact with an applied magnetic field. The diamagnetic material reduces the density of magnetic field lines, while the paramagnetic material concentrates the density of magnetic field lines.

homogenous field, move to regions of lower field strength (Figure 1.1). Diamagnetic molar susceptibilities (χ_D) are negative and typically range from -1 to -100 × 10^{-6} emu/mol. They are also independent of field strength and temperature.

Paramagnetism is exhibited by materials containing unpaired electrons which are weakly attracted to an externally applied magnetic field. When placed in a magnetic field, these materials concentrate the density of magnetic field lines around them or, in the case of a non-homogenous field, move to regions of higher field strength (Figure 1.1). In the presence of an external field, the individual spins align with the applied field; however, the individual spins become disordered and do not interact with each other magnetically when the external field is removed (Figure 1.2). Paramagnetic molar susceptibilities (χ_P) are positive and typically temperature dependent. Temperature independent paramagnetism (TIP) may exist in systems where there is a mixing of the ground (singlet) state with excited states that are not thermally populated. However, being on the order of 10^{-4}

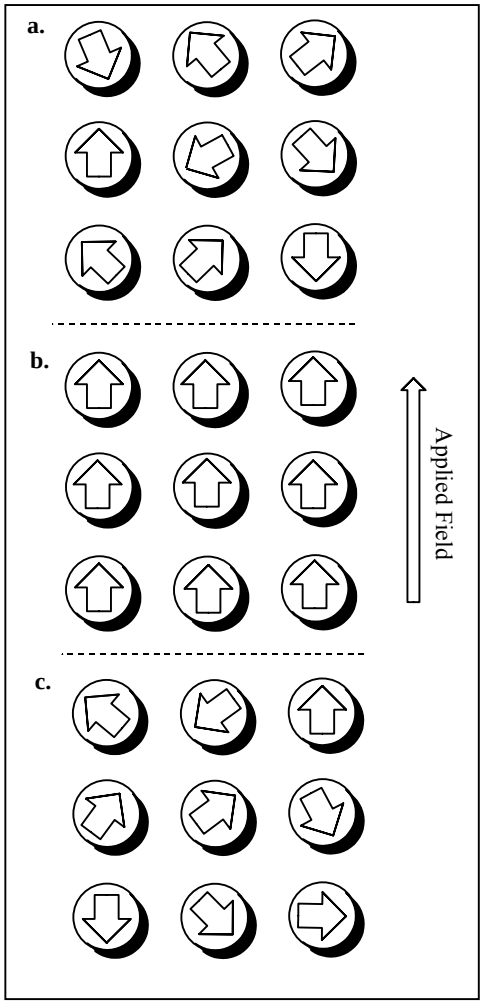

Figure 1.2 (a) Individual spins are randomly oriented and do not interact with each other in the absence of an external magnetic field. (b) When a strong enough external magnetic field is applied, the individual spins align with it. (c) When the external field is removed, the individual spins return to a random orientation with no interaction.

emu/mol, TIP is significantly smaller than temperature dependent paramagnetism at low temperatures.

Materials having unpaired electrons also have a number of filled electron shells which account for a diamagnetic contribution to their magnetic susceptibilities. The total magnetic susceptibility for a material is actually the sum of the paramagnetic and diamagnetic susceptibilities:

$$\chi = \chi_P + \chi_D \qquad (2)$$

The total magnetic susceptibility can be obtained by direct measurement. The paramagnetic susceptibility can then be found by subtracting out the diamagnetic susceptibility, sometimes referred to as the diamagnetic correction. Diamagnetic susceptibilities of atoms in molecules are additive and can be estimated using Pascal's constants. Using this method, χ_D of each individual atom and other constitutive corrections such as π-bonding are added to get the total diamagnetic susceptibility. Another possible method of obtaining the diamagnetic correction is to measure the diamagnetic susceptibility of a model compound. This is applicable when dealing with materials with a large diamagnetic contribution.

2. Curie Law

In 1895, Curie showed that paramagnetic susceptibilities could be related to temperature by the Curie Law:

$$\chi = \frac{C}{T} \qquad (3)$$

In this equation, χ refers to the paramagnetic molar susceptibility (χ_P), with the assumption that the diamagnetic correction has been made. C is the Curie constant and T

is the absolute temperature. This equation shows the inverse relationship between χ and T and also allows for relating M and H:

$$\chi = \frac{C}{T} = \frac{M}{H} \qquad (4)$$

From this expression, it is evident that magnetization decreases as temperature increases, since thermal agitation works to keep the individual magnetic moments randomly oriented. If the temperature is increased, χ also decreases because the magnetization is decreased. When the applied field is increased, it works against thermal agitation to align the individual magnetic moments thus increasing magnetization.

The Curie constant can be experimentally determined by plotting χ^{-1} vs. T, where the slope equals C^{-1}. The Curie constant can be defined with the following equation:

$$C = \frac{Ng^2\mu_B^2 S(S+1)}{3k} \qquad (5)$$

In this equation, N is Avogadro's number (6.0220×10^{23} mol^{-1}), g is the Landé factor, μ_B is the Bohr magneton (9.274×10^{-24} J/T), k is the Boltzmann constant (1.3807×10^{-23} J/K), and S is the electron spin (S = ½ per electron). The Landé factor is the gyromagnetic ratio of the orbital magnetic moment which expresses the proportionality between angular and magnetic moments. When the total angular momentum is zero, g is equal to 2.0023, however, the presence of an orbital contribution can change this value.

Either the effective magnetic moment (μ_{eff}) or χT of a material is often used to describe the magnetic properties. The effective magnetic moment can be defined by the following equation:

$$\mu_{eff} = \sqrt{\frac{3k\chi T}{N}} = 2.83\sqrt{\chi T} \qquad (6)$$

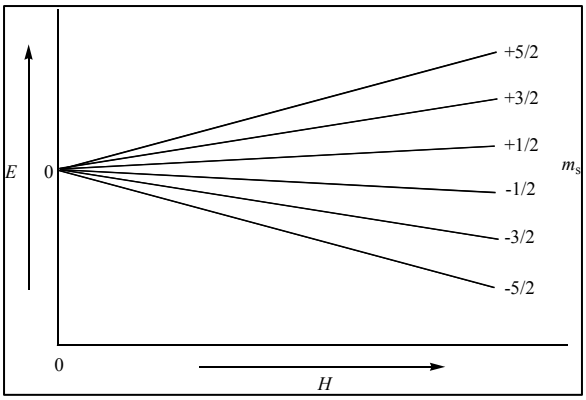

Figure 1.3 Octahedral Mn(II) has *S* = 5/2 and *L* = 0 leading to 6 degenerate states (2*S* + 1 = 6) which are split in a magnetic field.

In a simple system of non-interacting spins where θ = 0 K, μ_{eff} is temperature independent and can be described by the following equation:

$$\mu_{eff} = \mu_B \sqrt{g^2 S(S+1)} \qquad (7)$$

The Curie Law can be arrived at by considering how the spin states are energetically affected by an applied magnetic field. For an atom or ion with spin m_s, there are a number of degenerate ground states ranging from $-S$ to S in steps of unity. The degeneracy of these sub-states is resolved upon application of a magnetic field to yield an equivalent number of sublevels (Figure 1.3). The energy of each sublevel, n, can be defined by:

$$E_n = m_s g \mu_B H \qquad (8)$$

The magnetic moment of each sublevel can be defined by:

$$\mu_n = -m_s g \mu_B = -\frac{\partial E_n}{\partial H} \qquad (9)$$

And the total magnetization, for all sublevels is:

$$M = -\frac{\partial E}{\partial H} \qquad (10)$$

Considering N total particles with n_s in the S sublevel the following Boltzmann expression applies:

$$P_S = \frac{n_S}{N} = \frac{\exp(-E_i / kT)}{\sum_S \exp(-E_i / kT)} \qquad (11)$$

Now the molar macroscopic magnetization of sample can be expressed by:

$$M = N\sum_{S} \mu_S P_S \qquad (12)$$

Summation of m_s over the range of $-S$ to S yields:

$$M = Ng\mu_B S B_S(x) \qquad (13)$$

In the above equation, $B_S(x)$ is the Brillouin function defined by:

$$B_S(x) = \frac{1}{S}\left[\left(S+\frac{1}{2}\right)\coth\left(S+\frac{1}{2}\right)x - \frac{1}{2}\coth\frac{x}{2}\right] \qquad (14)$$

The dimensionless parameter x is the ratio of magnetic energy, which tends to align the magnetic moments, to the thermal energy which tends to keep the system randomly oriented:

$$x = \frac{g\mu_B H}{kT} \qquad (15)$$

There are two limiting regions of the Brillouin function, when $x >> 1$ and $x << 1$. When $x >> 1$:

$$B_S(x) = \frac{1}{S}\left[\left(S+\frac{1}{2}\right) - \frac{1}{2}\right] = 1 \qquad (16)$$

So the magnetization can be written as:

$$M = Ng\mu_B S \qquad (17)$$

That equation describes the saturation magnetization (M_s). This is the point where the thermal energy is overcome by the applied magnetic field and all magnetic moments are aligned with the field.

The other limiting region of the Brillouin function is when $x << 1$. The following now describes the Brillouin function:

$$B_S(x) = \frac{(S+1)x}{3} \qquad (18)$$

Now, since $\chi = M/H$, the following expression can be written:

$$\chi = \frac{M}{H} = \frac{Ng^2\mu_B^2 S(S+1)}{3kT} \qquad (19)$$

The above equation is the Curie Law which describes spin-only magnetism. When there is a significant orbital contribution, as with transition metals beyond the first row, the orbital angular momentum must be taken into consideration. This will be discussed after defining the Curie-Weiss Law.

3. Curie-Weiss Law

The Curie Law describes the magnetic behavior of *ideal* paramagnetic materials very well, however, it can not accurately describe systems when intermolecular interactions are involved. A simple modification to the Curie Law, based on molecular field theory, is used to describe materials in which the magnetic spins experience some type of effective parallel or antiparallel exchange field due to cooperative interactions with neighboring spins.

The molecular field theory states that the presence of ordering interactions between spins can be accounted for by considering the effective internal magnetic field (H_m), which was originally termed *molecular field* by Weiss. The molecular field can be defined by:

$$H_m = \gamma M \qquad (20)$$

Where:

$$\gamma = \frac{2zJ}{Ng^2\mu_B^2} \qquad (21)$$

Here, z is the number of nearest neighbors around a magnetic spin and J is the interaction parameter between two nearest neighbor spins. The sign of J may be positive or negative depending on whether the spins align parallel (+) or antiparallel (-).

Now, the actual magnetic field that acts upon the magnetic moments (H_T) can be defined as:

$$H_T = H + \gamma M \qquad (22)$$

This expression can be substituted into the x parameter of the Brillouin function, taking the place of H, which leads to the Curie-Weiss Law:

$$\chi = \frac{M}{H} = \frac{C}{T - \theta} \qquad (23)$$

Where:

$$\theta = \gamma C \qquad (24)$$

The addition of this correction factor to the Curie Law is called the Weiss constant (θ). The Weiss constant has units of temperature and may be positive or negative depending on the type of interactions taking place. Positive values are representative of dominant ferromagnetic (parallel) coupling, while negative values are representative of dominant antiferromagnetic (antiparallel) coupling. The magnitude of θ, in either the positive or negative direction, is indicative of the strength of the intermolecular interactions between spins.

4. Van Vleck's Equation

Some magnetic systems are not completely described by spin-only magnetism. There may be a significant orbital contribution to the magnetic moment or magnetic anisotropy may be present. A common source of anisotropy is zero-field splitting where

the degenerate ground states are partially resolved in the absence of an external field. The partially resolved states are separated by the zero-field splitting parameter, 2*D*, described by units of Kelvins. A general method for calculating magnetic susceptibilities affected by these variables is Van Vleck's equation, which takes the energy levels of accessible states into consideration.

The first step in derivation of this equation is expanding the energy terms according to the increasing powers of the applied field:

$$E_n = E_n^0 + HE_n^{(1)} + H^2 E_n^{(2)} + \ldots \qquad (25)$$

Here, E_n^0 is the energy of level *n* in zero applied field, $E_n^{(1)}$ is the first-order Zeeman term linear in *H*, and $E_n^{(2)}$ is the second-order Zeeman term in H^2. Expansion of the energy to the second-order is usually sufficient. The first term, E_n^0, makes no contribution to the moment of a given state. The contribution of the first-order Zeeman term is independent of field strength, while the contribution of the second-order Zeeman term is field-dependent. Since:

$$\mu_n = -\frac{\partial E_n}{\partial H} \qquad (26)$$

an expression can be written for μ_n based on the energy expansion:

$$\mu_n = -E_n^{(1)} - 2HE_n^{(2)} \qquad (27)$$

The exponential in the equation for the total magnetic moment of a system (*M*) stated earlier can be rewritten (for small values of *H*) as:

$$\exp(-E_n / kT) = (1 - HE_n^{(1)} / kT)\exp(-E_n^0 / kt) \qquad (28)$$

Now, the total magnetization can be rewritten as:

$$M = N\frac{\sum_n(-E_n^{(1)} - 2HE_n^{(2)})(1 - HE_n^{(1)}/kT)\exp(-E_n^0/kT)}{\sum_n(1 - HE_n^{(1)}/kT)\exp(-E_n^0/kT)} \qquad (29)$$

When considering paramagnetic systems where there is no magnetization in zero applied field, the following applies:

$$\sum_n -E_n^{(1)}\exp(-E_n^0/kT) = 0 \qquad (30)$$

And:

$$M = NH\frac{\sum_n[(E_n^{(1)})^2/kT - 2E_n^{(2)}]\exp(-E_n^0/kT)}{\sum_n\exp(-E_n^0/kT)} \qquad (31)$$

Since $\chi = M/H$, the magnetic susceptibility can be described by the following:

$$\chi = N\frac{\sum_n[(E_n^{(1)})^2/kT - 2E_n^{(2)}]\exp(-E_n^0/kT)}{\sum_n\exp(-E_n^0/kT)} \qquad (32)$$

From this equation, the magnetic susceptibility is determined by taking a population-weighted average of the susceptibility of a specific level.

5. Bulk Magnetic Properties

In paramagnetic materials, the magnetic spins are essentially independent spins acted upon only by the applied magnetic field. In the presence of the applied field, the spins tend to align parallel to the field, but since they are independent spins, thermal agitation ensures a random orientation when the applied field is removed. Often, however, the individual spins interact with neighboring spins in a cooperative fashion where the direction of one spin influences the directions of its neighboring spins. These interactions are short-ranged and only important between nearest neighbors, but, in bulk,

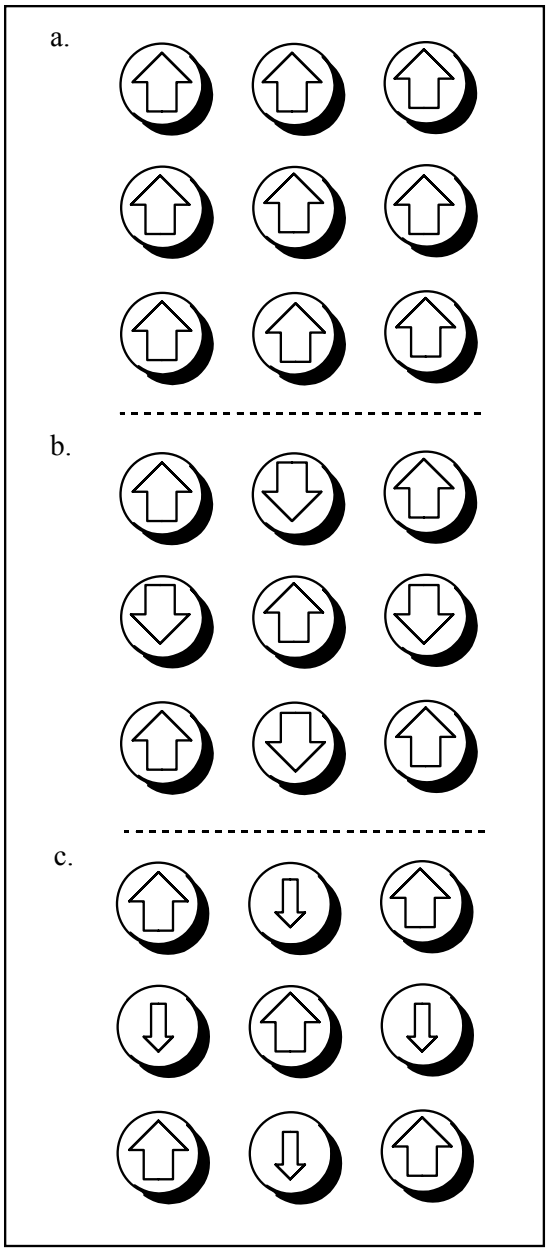

Figure 1.4 (a) Below the T_C and in zero magnetic field, unpaired electron spins in a ferromagnet are all ferromagnetically coupled, i.e. neighboring spins align in a parallel fashion. (b) Below the T_N and in zero magnetic field, unpaired electron spins in an antiferromagnet are all antiferromagnetically coupled, i.e. neighboring spins align in an antiparallel fashion. (c) Ferrimagnets behave like antiferromagnets except that the neighboring spins are unequal which results in a net magnetic moment.

they can lead to long-range magnetic ordering in the absence of an applied field below a certain critical temperature. A few basic types of bulk magnetic properties will be defined, including ferromagnetism, antiferromagnetism, ferrimagnetism, and canted antiferromagnetism.

In ferromagnetic materials the spins align in the same direction below a certain critical temperature in the absence of an external magnetic field. In this type of material, the individual spins are ferromagnetically coupled to their neighboring spins meaning that the direction of one spin favors the parallel alignment of the neighboring spin(s). A ferromagnet consists of spins that are all aligned parallel (Figure 1.4). Above the critical temperature of ferromagnetic materials, referred to as the Curie temperature (T_C), they typically behave as paramagnets since the surrounding thermal energy is strong enough to overcome the strength of the

ferromagnetic coupling.

In antiferromagnetic materials, the spins of unpaired electrons align in an antiparallel fashion in the absence of an external magnetic field and below a certain critical temperature called the Néel temperature (T_N) (Figure 1.4). In antiferromagnets, the direction of an individual spin causes neighboring spin(s) to align in an antiparallel direction. This is referred to as antiferromagnetic coupling. Above the T_N, antiferromagnets typically behave as paramagnets, like ferromagnetic materials.

In a special case of antiferromagnetism, called ferrimagnetism, the magnetic moments are arranged antiparallel, however, the magnetic moments are not equal (Figure 1.4). This leads to net magnetization since the opposing moments do not cancel each other out. Ferrimagnets typically behave like paramagnets above the T_N (T_C is not used to describe the critical temperature since the main interactions in ferrimagnetic materials are antiferromagnetic).

Canted antiferromagnetism, sometimes referred to as weak ferromagnetism, is a magnetic state that is similar to ferrimagnetism since the spins are antiferromagnetically coupled and there is net magnetization below the T_N. However, the net magnetization does not arise from the presence of unequal and opposite spins, it arises from the canting of the magnetic moments by a few degrees.(Figure 1.5) Canting does not always lead to net magnetization since complete cancellation of spins can still occur depending on the orientation of sublattices.

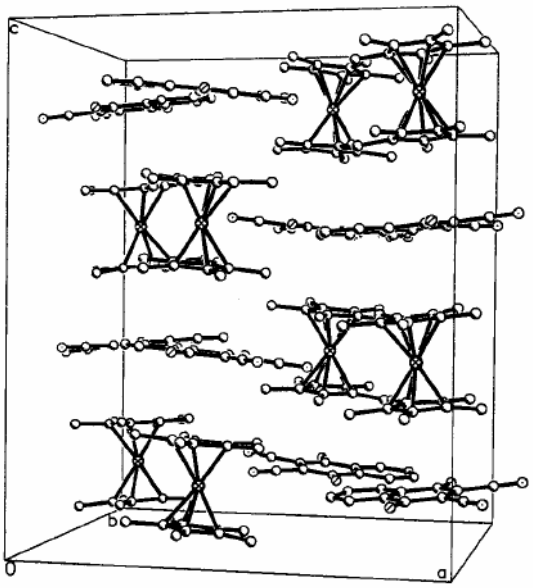

Figure 1.5 (Below) Each bold arrow represents the orientation of an individual spin. Due to cancellation there is no net magnetization in the *a* direction, however, there is a non-zero net magnetization in the *b* direction. (Left) The crystal structure of $[Fe(Cp^*)_2]^+[DCNQ]^-$,[1] which exhibits canted antiferromagnetism. The canting of the cations and anions, which each have one unpaired electron, is visible.

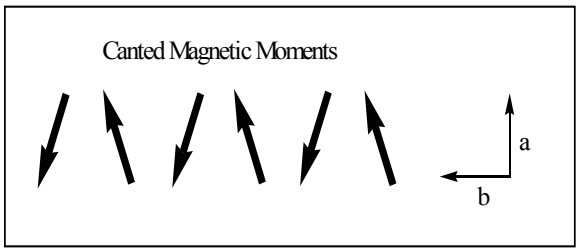

6. Magnetic Measurements

Using SQUID (Superconducting Quantum Interference Device) magnetometry, it is possible to measure the magnetization of a sample with a defined mass in various applied fields (up to 7 T) and at various temperatures (as low as 1.8 K). This data may be fit to the Curie Law, or Curie-Weiss Law, to yield information about bulk and molar magnetic properties. In addition to applying a static magnetic field, it is also possible to measure the magnetic susceptibility in an alternating (*ac*) field which allows some insight into the dynamics of a magnetic system.

Graphic representations of the temperature dependence of χ, as well as M vs. H plots, are useful in identifying the magnetic character of a material. When measuring the magnetization as a function of temperature in a constant applied field, it is possible to calculate the molar magnetic susceptibility. Plots of χ vs. T are shown for a simple paramagnet (θ = 0 K), a ferromagnetically-coupled material (θ = 1 K), and an antiferromagnetically-coupled material (θ = -1 K) (Figure 1.6). The plots are different based on their vertical asymptotes (dependent on θ), but the curves have the same shape

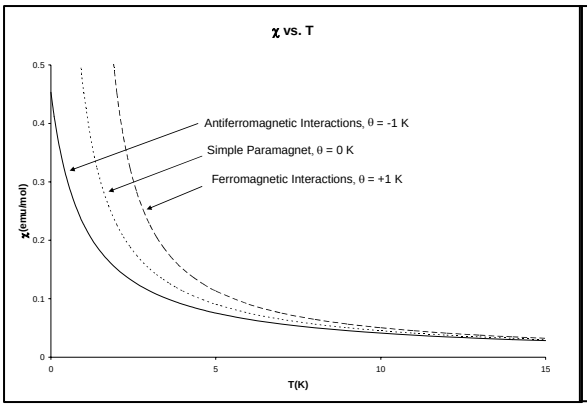

Figure 1.6 Plot of χ vs. T for a simple paramagnet, ferromagnetic-like material, and an antiferromagnetic material.

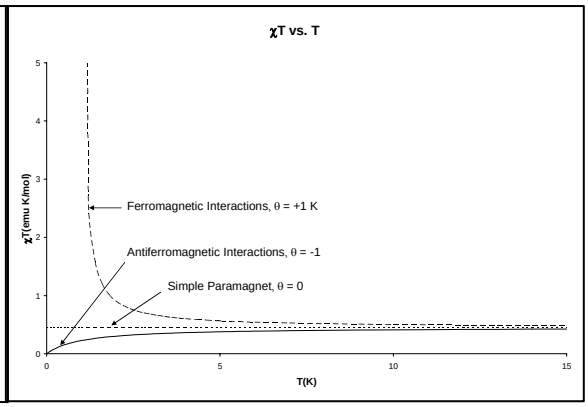

Figure 1.7 Plot of χT vs. T for the three materials represented in figure 1.6.

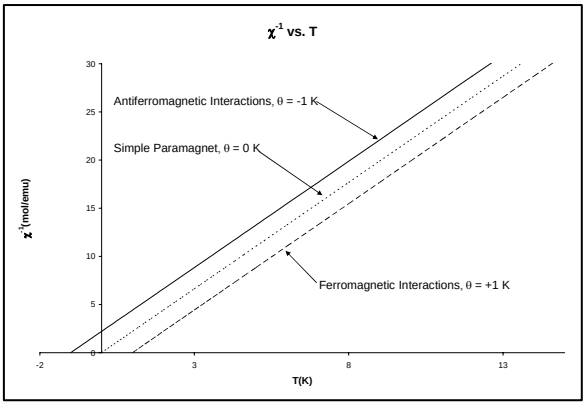

Figure 1.8 Plots of χ^{-1} vs. T for the three materials represented in figure 1.6.

which can be misleading. For that reason it is more informative to plot χT vs. T, which gives clearer evidence of the magnetic character (Figure 1.7). In this type of plot, the curve representing the ferromagnetically-coupled material curves up, the curve for the paramagnet is a horizontal line, and the curve for the antiferromagnetically-coupled material curves down. Example plots of χ^{-1} vs. T are also shown (Figure 1.8). Notice that the paramagnet has $\theta = 0$ K and its x-intercept = 0 K, the ferromagnetically-coupled material has $\theta = 1$ K and its x-intercept = 1 K, and the same relationship applies for the antiferromagnetically-coupled material. The Curie constant, as stated earlier, can be determined from the slope of χ^{-1} vs. T which is C^{-1}.

As mentioned above, plots of M vs. H (constant temperature) are also useful in magnetic characterization. Curves for each type of magnetic material all have representative shapes which are generalized in figure 1.9. A characteristic of the curves for ferromagnets, paramagnets, and ferrimagnets is the saturation magnetization (M_s).

This is the point where all of the magnetic moments in a material are aligned with the field, therefore the magnetization of the sample cannot increase any further. For a ferromagnet or paramagnet, the following equation stated earlier applies:

$$M_s = Ng\mu_B S \qquad (33)$$

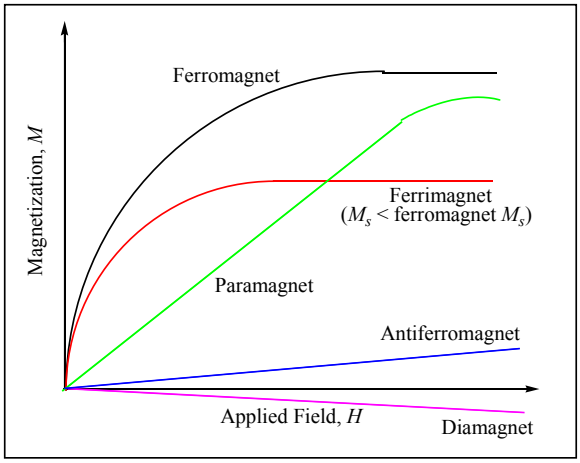

Figure 1.9 Examples of *M* vs. *H* curves for different types of magnetic materials.

In this equation N is Avogadro's number, g is the Lande constant, S is the spin state, and μ_B is the Bohr magneton. The saturation magnetization for a ferrimagnet can be expressed either of two ways depending on whether incomplete cancellation of the magnetic moments arises from differences in g or S, respectively:

$$M_s = N\Delta g\mu_B S \qquad (34)$$

$$M_s = Ng\mu_B \Delta S \qquad (35)$$

In these equations, Δg refers to the difference in the Lande constant for the two spins of unequal magnitude and ΔS refers to the difference in spin.

Another important topic for M vs. H plots is the presence of hysteresis. This is a memory effect that can be observed when the magnetization curve does not follow the same path forwards and backwards as the applied field is cycled from positive to negative (Figure 1.10). As the field is applied starting from zero field, the sample becomes magnetized (this segment of the curve is often omitted for clarity). As the field is lowered to zero, the sample retains some magnetization, which is referred to as the remanence. The sample remains magnetized until the applied field is strong enough in

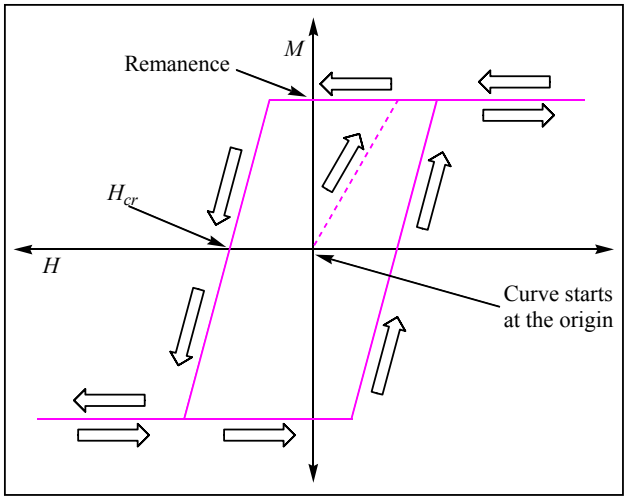

Figure 1.10 Plot of *M* vs. *H* that displays hysteresis.

the negative direction to flip the spins; this field strength is referred to as the coercivity or coercive field (H_{cr}). The hysteresis loop is typically centered on the origin since the behavior of the magnetization as the field is reversed follows the same pattern.

Plots of *M* vs. *H* also reveal whether the magnet in question is soft or hard. A soft magnet is magnetized when an external field is applied but it does not retain its magnetization when the applied field is removed. This translates into small values of coercivity and remanence. For an ideal soft magnet, the curve would follow the same path forwards and backwards as the applied field is oscillated as illustrated in figure 1.11. Hard magnets have large values of coercivity and remanence making them ideal for use as permanent magnets since they retain magnetization even when the applied field is removed. The curve in figure 1.10 is an example of a hard magnet, assuming it is on the same scale as the plot in figure 1.11.

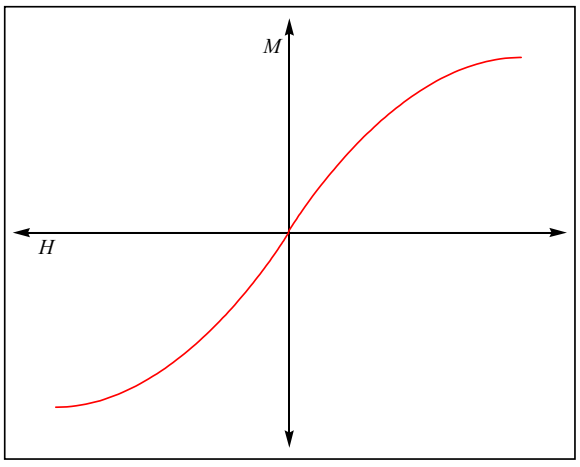

Figure 1.11 Representative plot of *M* vs. *H* for a soft magnet.

Metamagnetism is the presence of a field dependent phase transition from an antiferromagnetic to a ferromagnetic-like state. This can be illustrated by examining

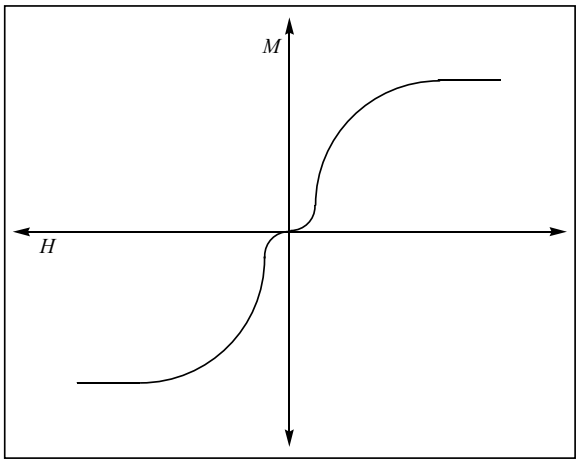

Figure 1.12 Representative plot of *M* vs. *H* for a metamagnet.

the *M* vs. *H* plot for a metamagnet at low enough temperature for spin interactions to be observed (Figure 1.12). The determining characteristic of this plot is the small slope of the curve around 0 G applied field which drastically increases at some field strength before leveling off in the stronger applied field. A small slope is indicative of antiferromagnetic interactions; the drastic increase in slope identifies the applied field strength at which ferromagnetic-like interactions take over.

The *M* vs. *H* data discussed up to this point has been based on a static (*dc*) magnetic field, where the magnetization at a given applied field is at thermal equilibrium. However, it requires a certain amount of time for a sample to adjust to any changes in the applied field. By using an alternating current (*ac*) to generate an alternating magnetic field, it is possible to measure the *ac* susceptibility, which gives some insight on the dynamics of a magnetic system.

7. ac Susceptibility

The *ac* magnetic field, H_{ac}, can be described by the following equation:

$$H_{ac} = H_0 \cos(\omega t) \qquad (36)$$

H_0 is the amplitude of the field, ω is the angular frequency ($\omega = 2\pi\nu$), and t is time. The magnetization of the sample, M_{ac}, lags behind H_{ac} since some time is required for the system to equilibrate. This can be written in the following terms:

$$M_{ac} = M_0 \cos(\omega t - \theta) \qquad (37)$$

In this equation, θ is the phase angle by which M_{ac} is shifted from the *ac* field. Using trigonometric relationships with the previous equations, the following can be written to describe the system:

$$M_{ac} = \chi' H_0 \cos(\omega t) + \chi'' H_0 \sin(\omega t) \qquad (38)$$

$$\chi' = \left(\frac{M_0}{H_0}\right)\cos\theta \qquad (39)$$

$$\chi'' = \left(\frac{M_0}{H_0}\right)\sin\theta \qquad (40)$$

There are two expressions that make up the *ac* susceptibility, χ' and χ", which can be defined with the following complex equation:

$$\chi_{ac} = \chi' - i\chi'' \qquad (41)$$

The real component, χ', is the in-phase component which can be referred to as the dispersion since it describes the dispersive magnetic response of the sample to the applied *ac* field. The imaginary component, χ", is the out-of-phase component which can be called the absorption since it refers to the energy absorbed by the system from the applied *ac* field. The characterization of magnetic properties is greatly dependent on the measurement of the *ac* susceptibility. Some of the uses for *ac* susceptibility include identification of spin-glass and magnetic phase transitions.

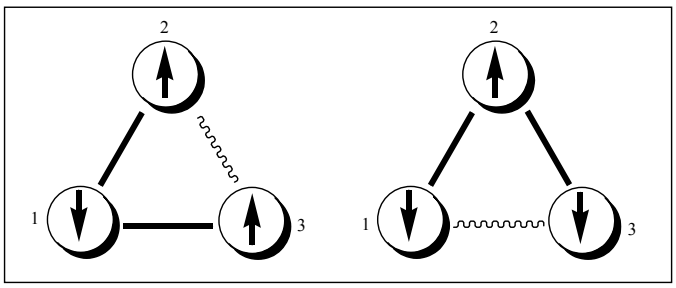

Figure 1.13 Each spin wants to be antiferromagnetically coupled to its nearest neighboring spin. Spin #3 cannot satisfy the coupling requirement for both of its neighboring spins (#1 and #2).

A spin-glass is a material that has some degree of magnetic frustration, and essentially is magnetically disordered, even at low temperatures. Frustration refers to the situation that arises when individual spins cannot satisfy the coupling requirements that their neighboring spins induce since the different neighboring spins are trying to force them in different directions. (Figure 1.13) This can be due to simple structural disorder or disordered magnetic doping to an otherwise ordered system. The *ac* susceptibility can indicate the degree of glassiness based on frequency dependence, meaning that the *ac* susceptibility at a given temperature changes as the frequency changes. On the other hand, frequency independent *ac* susceptibility indicates a lesser degree of glassiness.

The presence and character of magnetic phase transitions are also determined using *ac* susceptibilities. A ferromagnetic phase transition can be characterized by a peak in χ' and a non-zero χ" value. An antiferromagnetic phase transition can be characterized by a peak in χ' and no out-of-phase component. The be-

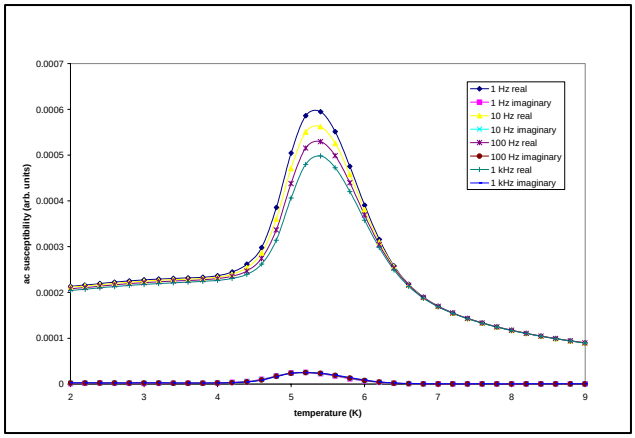

Figure 1.14 Plot of *ac* susceptibility vs. temperature displays frequency dependence and a peak in χ' accompanied by a non-zero χ" which gives evidence for some degree of disorder or frustration as well as a ferromagnetic-like phase transition.

havior of χ" for ferromagnetic and antiferromagnetic phase transitions can be rationalized by considering that when a magnetic moment is present, as with the ferromagnetic case, the magnetic moment will oscillate. In this case, χ" refers to the energy absorbed by the magnetic moments adjusting to the oscillating field. The antiferromagnetic case will have a zero χ" value since there is no magnetic moment that needs to follow the oscillation of the magnetic field. An example of an *ac* susceptibility plot is shown in figure 1.14.

Chapter II: Metallocene-based Molecular Magnets

The study of metallocene-based molecular magnets began with the discovery of the charge-transfer (CT) salt ferromagnet [FeCp*$_2$][TCNE], T_c = 4.8 K, by Joel Miller et al.[2] The CT salt is formed by a one-electron transfer from decamethylferrocene to tetracyanoethylene where both the electron donor ($\mathbf{D}^+$) and the acceptor ($\mathbf{A}^-$) each have S = ½ which couple ferromagnetically. Further studies employing Mn(III) and Cr(III) in the place of Fe(III) also yielded new ferromagnets where $\mathbf{D}^+$ has S = 1 and 3/2, respectively.[3, 4] These discoveries launched efforts to find different one-electron organic acceptors other than TCNE, as well. The most interesting aspect of this work was the mode of magnetic interaction, which occurs *through-space* rather than through a chemical bond due to the lack of covalent bonding. The details of metallocene-based molecular magnets will be covered after a brief discussion of molecular magnetism and its history.

1. Molecular Magnetism

Molecular magnetism deals with the magnetic properties of isolated molecules and assemblies of molecules. There are a few striking differences between molecular magnets and traditional atom-based magnets. Atom-based magnetism can be defined by the presence of magnetic moments which reside on *d* or *f* orbitals of transition or lanthanide metals with extended bonding in at least two dimensions. Molecular magnets, on the other hand, have magnetic moments residing on *d* or *f* orbitals and either magnetic spins located in *s* and/or *p* orbitals or molecular orbitals which are important in mediating the magnetic interaction. The other key difference is the means for preparation of each

species. Atom-based magnets are typically synthesized using metallurgical processes under extreme conditions. Molecular magnets are prepared by low-temperature processes incorporating a combination of organic, organometallic, and coordination metal chemistry.

2. *Brief History of Molecular Magnetism*

Molecular magnetism has a relatively recent history, with most of the significant developments occurring in the late 20th century. The roots of molecular magnetism can be traced back to studies of magnetic exchange coupling in metal oxides and other continuous lattice compounds during the 50's and 60's. Anderson, Goodenough, and Kanamori were among those who rationalized exchange coupling in species such as transition metal oxides by considering orbital symmetry.[5-7] This new insight into magnetic coupling provided the foundation for the study of structure-property relationships in magnetic materials.

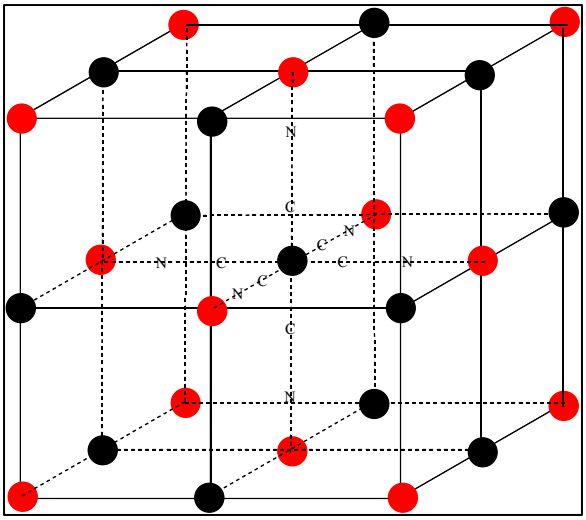

Figure 2.1 Face-centered cubic structure of Prussian blue type materials with the black dots referring to the high-spin metal centers and the red dots referring to the low-spin metal centers. The repeating orientation of the bridging cyanides is shown around the central metal ion.

Also during the 50's and 60's, studies were being conducted on the Prussian blue-type magnets. Prussian blue ($Fe^{III}_4[Fe^{II}(CN)_6]_3 \bullet 15H_2O$) was found to exhibit bulk ferromagnetism at low temperatures (5.6 K).[8, 9] The general structure for this type of compound is

shown in figure 2.1. Further structural studies over the years has led to the development of other Prussian blue-type compounds with different transition metals that exhibit long-range order at higher temperatures, such as $V^{II}[Cr^{III}(CN)_6]_{0.86}$•2.8 H_2O which orders at 315 K.[10] The bulk magnetism is typically ferrimagnetism resulting from incomplete cancellation of antiparallel spins, but may be ferromagnetic in some cases.[11]

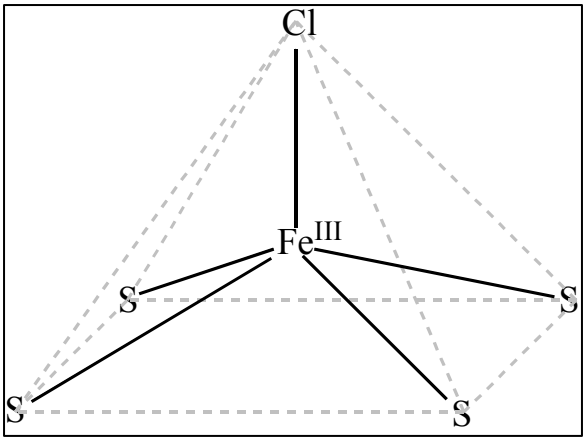

Figure 2.2 Square-pyramidal geometry around the Fe(III) center which leads to *S* = 3/2.

Other magnets from coordination compounds and organometallic complexes were beginning to be discovered in the 1960's. Some highlights of molecular magnetism research during the latter half of the 20th century include the following: Wickman et al. published their work on bis-(*N*,*N*-diethyldithiocarbamato-Fe(III) chloride in 1967 reporting it to be a spin 3/2 ferromagnet below 2.5 K.[12] The presence of a spin 3/2 ground state for iron(III) was different than the typical high-spin $S = 5/2$ or low-spin $S = 1/2$ compounds at the time. It was tentatively explained by the square pyramidal structure around the metal center leading to a spin quartet ground configuration (Figure 2.2). The magnetic data supported the $S = 3/2$ spin state, however, a detailed explanation of the electronics of the system had yet to be offered. In 1970, Barraclough reported work on manganese(II) phthalocyanine, another $S = 3/2$ compound (Figure 2.3).[13] Magnetic anisotropy measurements were employed on this square planar compound to help deduce the electronic structure and explain its bulk ferromagnetic behavior at low

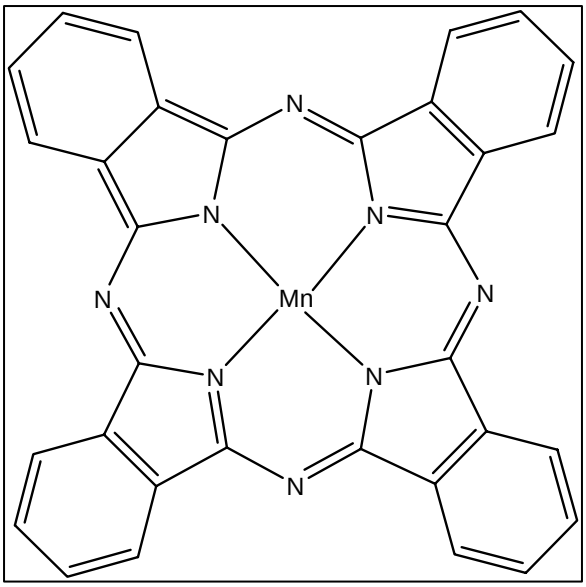

Figure 2.3 Planar structure of manganese (II) phthalocyanine.

temperatures. The importance of Wickman's and Barraclough's work was the pioneering methods employed by each to draw a structure-property relationship in reference to magnetic properties.

Through the 70's, layer perovskite salts of Cu(II) were discovered to be useful models for ferromagnetism in insulating 2-D lattices.[14] Later, Cr(II) analogs were shown to be ferromagnets at temperatures as high as 60 K. The significance in these materials is that the inorganic layers are separated by organic cations which can be varied in size to control the spatial dimensionality of the magnetic exchange (Figure 2.4).[15] Essentially, the bulk magnetic character can be controlled by altering the size or shape of the organic cations. Direct structure-property relationships like these are important elements in the ability to synthesize "designer" magnets with specific magnetic properties which is the focus of much magnetic research today.

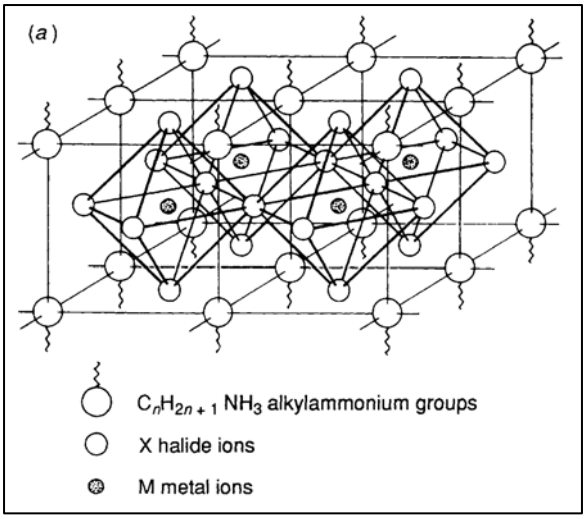

Figure 2.4 Typical layer perovskite salt example showing one layer of $(NRH_3)_2MX_4$. The separation of adjacent layers is dependent on the length of the alkyl group.

In the 80's, Miller et al. discovered that the charge transfer [FeCp*$_2$][TCNE] is a ferromagnet with T_c = 4.8 K. This

proved to be an interesting discovery since the magnetic coupling does not occur *through-bond* but *through-space*. In the early 90's, the 3-D coordination polymer $V[TCNE]_x \bullet yCH_2Cl_2$ was discovered to magnetically order near room temperature.[16] The structure of this material is yet to be understood fully, but the prospect of magnetic materials ordering temperatures at or near room temperature places these materials at the forefront of modern molecular magnetism. Currently, Miller's focus lies in 3-D molecular magnets such as $M(acceptor)_y$ coordination polymers on which he has published several articles over the past few years.[17-19]

Some important contributors to the field of molecular magnetism over the past quarter century include Olivier Kahn, William Hatfield, Roger Willett, Dante Gatteschi, and Michel Verdaguer, among others. Oliver Kahn performed extensive studies on how to obtain molecular magnets through high spin transition metal complexes. These included 1-D ferrimagnetic chains of *o*-phenylenebis(oxamato)cuprate ($[Cu(opba)]^{2-}$) and M^{2+} where the interaction between M^{2+} ($S = 5/2$ for Mn^{2+}, for example) and Cu^{2+} ($S = ½$) is antiferromagnetic but there is net magnetization due to incomplete cancellation of the spins.[20] Later, Kahn also looked at the connection between optical and magnetic properties, as well as the photomagnetic properties of molecular magnets.[21-23] He is also the author of *Molecular Magnetism*, a definitive book on theoretical and experimental fundamentals of the field.

William Hatfield's most notable contribution to molecular magnetism was the discovery of correlation between a simple structure parameter and exchange coupling in di-μ-hydroxo copper (II) complexes in collaboration with Derek Hodgson.[24] This work inspired others to formulate more complete quantum mechanical analyses for explaining

exchange coupling.[25] Hatfield also studied other dimer systems with the focus of identifying magnetostructural correlations.[26, 27] Roger Willett and Dante Gatteschi have also extensively studied magnetostructural correlations; Willet with oligomers and polymers of copper halide salts and Gatteschi with low-symmetry transition metal complexes and large spin clusters. Willett's work is focused on layer perovskite structures of copper halides which allows for a variety of interactions between the metal centers through different bridging modes as well as 2-D and 3-D interactions.[28-31] Gatteschi continues to study synthetic methods for obtaining molecular magnets as well as investigation of single molecule magnets.[32-34] Also, Michel Verdaguer has contributed significant research on the synthesis of molecular magnets with interesting optical and photomagnetic properties, as well as collaborations with Kahn and Gatteschi.[20, 35-37]

3. Magnetic Exchange Interactions

Exchange interactions between magnetic centers are important in understanding the magnetic properties of molecular magnets. There are four types of exchange coupling which are based on extent of delocalization of the magnetic moments as well as the metallic or non-metallic character of the material. These are direct exchange, superexchange, indirect exchange, and itinerant exchange. In direct exchange and superexchange, the magnetic moments are strongly localized on the metal centers and interact either directly through space or bridging diamagnetic ligands. Indirect exchange is the coupling of localized magnetic moments on metals centers with conduction electrons and itinerant exchange is the coupling between conduction electrons. Indirect

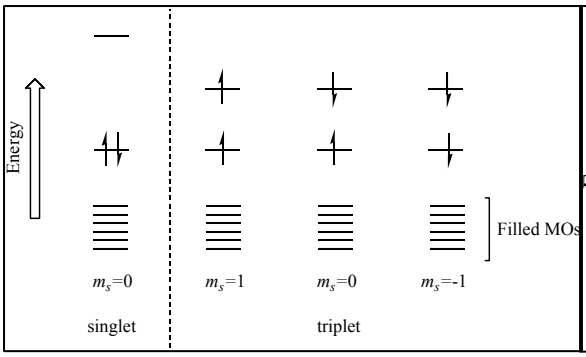

Figure 2.5 The singlet and triplet spins states that can arise with exchange coupling.

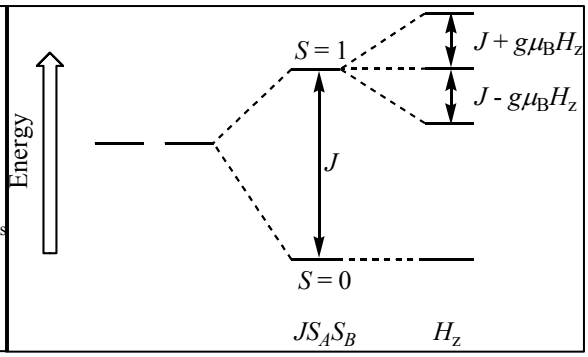

Figure 2.6 Splitting diagram for the singlet and triplet states with relative energies in an external applied magnetic field.

and itinerant exchange are not as important to this discussion since molecular magnets are not typically electrically conductive. The most relevant types of exchange interaction in molecular magnets are direct exchange and superexchange. In direct exchange, the exchange occurs directly through the interactions of the orbitals of two metals with magnetic moments. In superexchange, the interaction between the metal centers occurs through ligand orbitals.

Exchange coupling can be rationalized by considering a simple system consisting of two identical transition metal centers, each with one electron in a non-degenerate orbital. The interaction between the two unpaired electrons can be described by the Heisenberg Hamiltonian:

$$\hat{\mathrm{H}} = -J\hat{S}_A \cdot \hat{S}_B \qquad (42)$$

In this equation, J is referred to as the isotropic interaction parameter or coupling constant between the two unpaired electrons and is the energy difference between the triplet and singlet states (Figure 2.5 and 2.6). Positive values of J are indicative of ferromagnetic interactions while negative values represent antiferromagnetic interactions.

The coupling of the two electron spins can result in either a spin singlet ($S = 0$), which is antiferromagnetic, or a spin triplet ($S = 1$), which is ferromagnetic. The energy difference between the singlet and triplet states is:

$$J = E_T - E_S = -2K_{AB} + \frac{(\varepsilon_1 - \varepsilon_2)^2}{J_{AA} - J_{AB}} \qquad (43)$$

In this equation, K_{AB} is an exchange integral, ε_1 and ε_2 are the energies of ψ_1 and ψ_2 (see figure 2.7), and J_{AA} and J_{AB} are one- and two-center Coulomb repulsion integrals. The key point is that when ψ_1 and ψ_2 are degenerate, the second term becomes zero and $J > 0$ which signifies a ferromagnetic interaction. However, when ψ_1 and ψ_2 are non-degenerate, the second term dominates and $J < 0$ signifying an antiferromagnetic interaction.

It should be noted that the magnetic moments may not be completely localized on the metal centers and some spin density can be found in bridging ligand orbitals which is the case with superexchange. Thus, the magnetic orbitals (functions describing these two

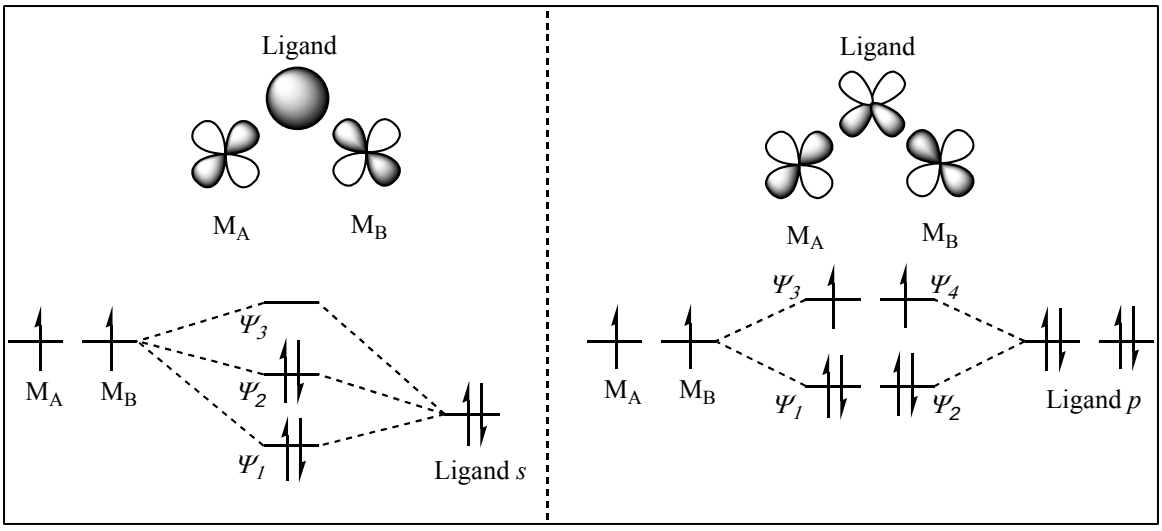

Figure 2.7 MO diagram for the interaction of two d^9 metal centers through a diamagnetic ligand by orbital overlap of metal *d* orbitals with (left) a filled ligand *s* orbital leading to antiferromagnetic coupling and (right) with two filled orthogonal ligand *p* orbitals leading to ferromagnetic coupling.

electrons) actually will contain some ligand orbital character. This is illustrated in the figure, where exchange occurs through an *s* or two orthogonal *p* ligand orbitals (Figure 2.7). The bridging angle determines how much *s* and *p* character is contributed to the bond between the metals and bridging ligand which accounts for the dominance of antiferromagnetic or ferromagnetic interactions respectively.

A simple example of exchange coupling is the interaction between two $S = ½$ copper ions in bridged copper (II) complexes.[24] In these materials, the ligand orbitals mediate the magnetic exchange so that the sign of the magnetic interaction is dependent on the Cu-O-Cu bond angles. Two situations can arise based on which ligand orbital is mediating the exchange as illustrated. When the bond angle is 90°, the *p* orbitals of oxygen are more prominent in the exchange and ferromagnetic interactions are predicted (Figure 2.7 right). However, as the bond angle increases to 180°, there is more *s* character in the hybrid orbital used in the exchange and antiferromagnetic interactions are predicted (Figure 2.7 left). Extensive structure-property information has been compiled on related compounds which show a linear correlation with Cu-O-Cu bond angles and corresponding values of *J*.[38] The data suggests that for angles less than 96°, a ferromagnetic interaction is expected while as the angle increases to 180°, stronger antiferromagnetic interactions are expected.

Exchange models, such as above, are important in describing molecular magnetism where the magnetic interaction occurs *through-bond*, however, charge-transfer salt magnets lack the covalent interactions necessary for such models to be applicable. A discussion of more relevant models for these systems will be discussed

later. Also, an extensive discussion of general molecular magnets will not be included. The focus will now be specifically on metallocene-based molecular magnets.

4. Metallocene-based Molecular Magnets

Several properties of the metallocenes (MCp_2) of the first row transition metals make them ideal as electron donors for CT salt magnets. These include good solubility in common organic solvents, commercial availability, symmetry, size, and redox properties. The fivefold symmetry of the Cp rings gives rise to orbital degeneracy which is favorable for ferromagnetism; lowering the symmetry tends to create a situation where electrons would rather be paired. The size is important in the stacking arrangement of the donors and acceptors in the 3-D structure which will be more apparent after further discussion. Also, based on the electrochemistry, a particular donor with a specific reduction potential will theoretically react with any organic electron acceptor that is sufficiently oxidizing.

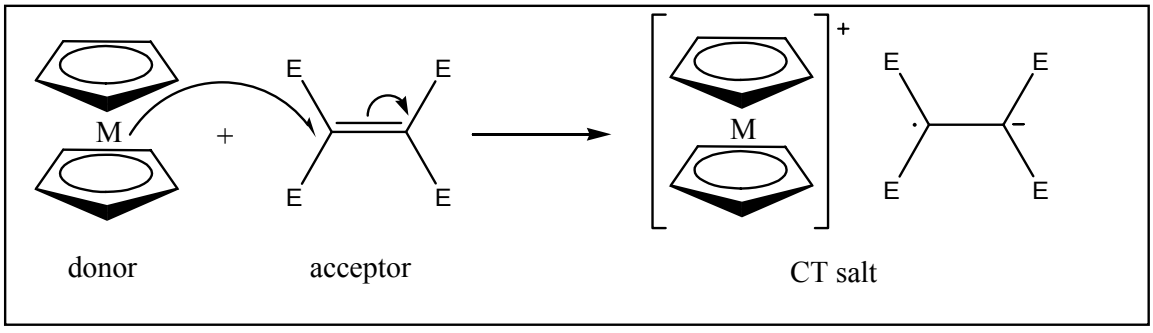

Figure 2.8 Formation of CT salt by electron transfer from a metallocene donor to an organic acceptor, E = electron withdrawing group. There are unpaired electrons on both the metallocenium ion (the quantity of which is determined by the identity of the metal, *M*) and the radical anion, which has one.

This makes decamethyl-metallocenes (MCp^*_2) even more attractive since their one electron reduction potentials are more negative than their corresponding metallocene counterparts by approximately 0.5 V.

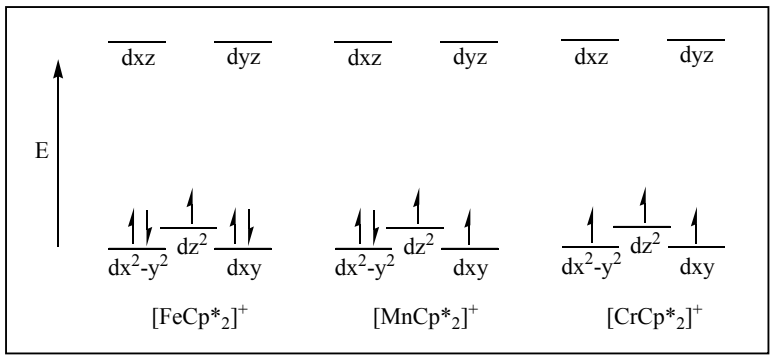

Figure 2.9 Metal orbital and electron configurations for each decamethylmetallocenium ion.

The main focus of research has been with salts of $FeCp^*_2$, $MnCp^*_2$, and $CrCp^*_2$ since they have reasonable reactivity and the oxidized species have unpaired electrons. The organic acceptors, upon accepting an electron, form radical anions (Figure 2.8) which give them a spin state (*S*) of ½. The resulting CT salt is composed of two non-covalently bonded species each having unpaired electrons ($[FeCp^*_2]^+$, S = ½; $[MnCp^*_2]^+$, S = 1; $[CrCp^*_2]^+$, S = 3/2) (Figure 2.9) which magnetically couple by through-space interactions.

The synthesis of the CT salts of MCp^*_2 (M = Fe, Mn, Cr) and organic acceptors is a relatively simple procedure. The donor ($\mathbf{D}^+$) and acceptor ($\mathbf{A}^-$) readily react in CH_2Cl_2 solution to form the CT salt which is precipitated by the addition of a non-polar solvent such as diethyl ether. The precipitate is collected and washed with ether to remove any un-reacted starting materials. With the exception of some decamethylferrocene salts, the other donors and their salts are not typically stable in air and require an inert atmosphere. Also, the synthesis of CT salts with $MnCp^*_2$ requires a special low temperature procedure since these salts are not stable at room temperature in solution. The choice of

solvent for the reaction is also important in the syntheses. The bulk of this type of research has used three reaction solvents in particular: methylene chloride (CH_2Cl_2), tetrahydrofuran (THF), and acetonitrile (MeCN). The use of different solvents to produce a specific CT salt has produced some interesting results. For example, when reacting $FeCp^*_2$ and tetracyanoethylene (TCNE), the product is $[FeCp^*_2][TCNE]$; however, when using MeCN in the reaction the product is $[FeCp^*_2][TCNE]\cdot MeCN$.[2] The role of the solvent is not completely understood; it may serve as filler for empty space between the donor-acceptor stacks in the case that the donor and acceptor are different sizes.

When studying these CT salts, it is extremely useful to have a crystal structure. Most CT salts of the form $[MCp^*_2][acceptor]$ had been found to follow a particular structural motif of alternating donor-acceptor ($\mathbf{D^+A^-}$) stacks in the π stacking direction to form 1-D chains in the solid state. These unit cells typically have two pairs of chains in which each pair is in-registry with respect to the two chains of the pair, and out-of-registry with respect to the other pair (Figure 2.10). This structure provides for the dominant intrachain spin coupling (J_{intra}), which is usually ferromagnetic ($J > 0$), and the less dominant interchain spin coupling (J_{inter}), which may be ferro- or antiferromagnetic. In the case of antiferromagnetic interchain interactions ($J < 0$), there exists a competition

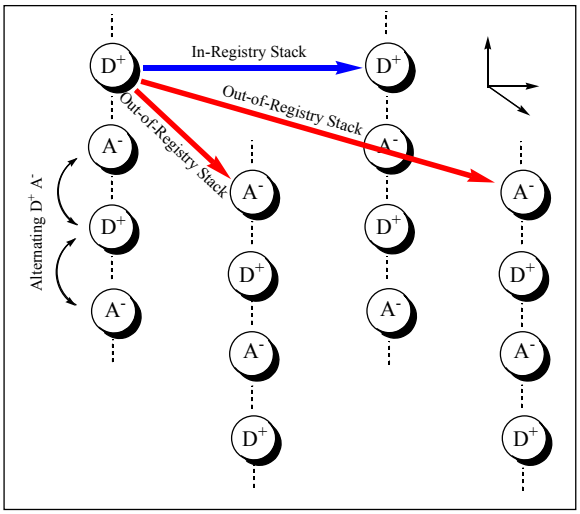

Figure 2.10 Alternating $\mathbf{D^+A^-}$ stacking pattern showing in-registry and out-of-registry chains.

between ferro- and antiferromagnetic forces that determines the bulk magnetic character of the material. The bulk character may be rationalized by the intra- and interchain distances between magnetic centers and the degree of registry with respect to adjacent chains within the material, both affecting the values of J_{intra} and J_{inter}.

5. Mechanism of Magnetic Coupling in CT Salts

There is some controversy surrounding the mechanism of magnetic coupling in CT salt magnets. The first attempt to explain the ferromagnetic interactions in [FeCp*$_2$][TCNE] involved the admixing of a virtual CT excited state with a ground-state model originally proposed by McConnell for chain structures comprised of alternating radical cation donors and radical anion acceptors.[39] This model, referred to as the McConnell-II model, essentially predicts antiferromagnetic interactions for donors and acceptors with non-degenerate partially occupied molecular orbitals (POMOs), but ferromagnetic interactions are possible with the presence of degenerate POMOs. This works for predicting the ferromagnetic interactions present in [FeCp*$_2$][TCNE] and [MnCp*$_2$][TCNE] but fails for [CrCp*$_2$][TCNE] since it predicts antiferromagnetic interactions.[40]

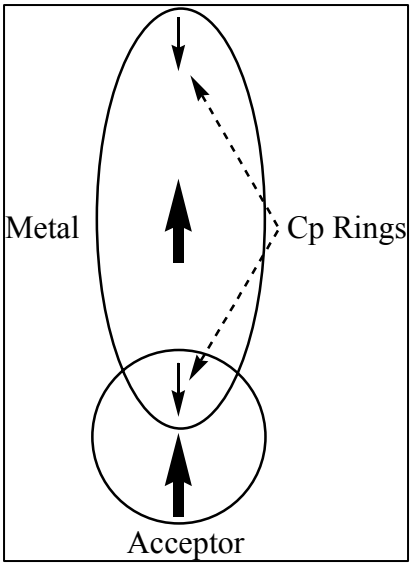

Figure 2.11 Overlap of postitive spin density on the metal induces negative spin density on the Cp rings which, through overlap, induces positive spin density in the magnetic orbital of the acceptor resulting in ferromagnetic coupling of the metal center and acceptor.

Kollmar and Kahn suggested the aforementioned model was an oversimplified picture of the magnetic

exchange and offered a more descriptive analysis demonstrating that the ground state of the donor-acceptor pair can actually be a singlet (antiferromagnetic) even if the lowest energy excited state is a triplet (ferromagnetic).[41] Another idea that has been offered, called the McConnell-I model, considers the exchange interaction involving a spin polarization effect where the positive spin density on the metal can induce negative spin density on the Cp rings through configurational mixing.[42] The negative spin density on the Cp rings overlaps areas of positive spin density on the acceptor within the stack which contributes to ferromagnetic coupling between the metal and acceptor (Figure 2.11). However, computational studies on diradical paracyclophanes have shown that the McConnell-I model is not a complete explanation for these systems.[43] So, a sufficient theoretical model that completely describes these systems has yet to be discovered.

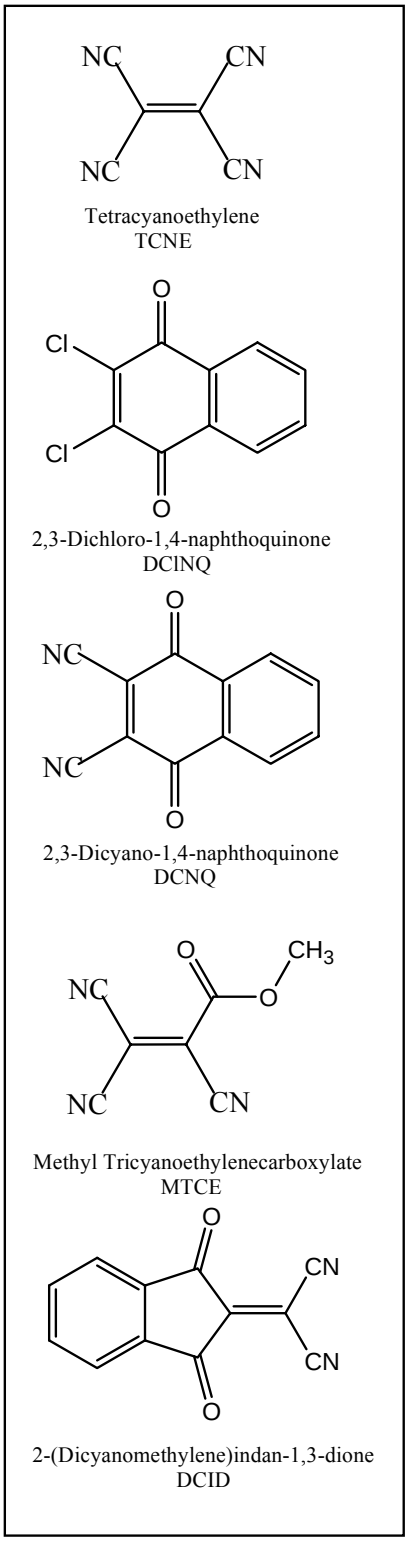

Figure 2.12 Structures of organic acceptors.

Organic Acceptors

The first MCp^*_2 CT salt discovered to have a ferromagnetic ground state was $[FeCp^*_2][TCNE]$.[2] The general structure of TCNE is a double bond

between two carbons surrounded by strong electron-withdrawing groups ($^{-}$C≡N) with an overall planar shape. The electron-withdrawing groups pull electron density from the π bond to help stabilize the radical anion formed after accepting an electron. The planarity of the acceptor maintains the short intrastack distance between the metal centers.

The structural backbone of TCNE has since been used in finding other organic acceptors for the synthesis of magnetic CT salts (Figure 2.12). 2,3-Dichloro- and 2,3-dicyano-1,4-naphthoquinone[1] (DClNQ and DCNQ), 2-(dicyanomethylene)indan-1,3-dione (DCID), and methyl tricyanoethylenecarboxylate (MTCE)[44] are a few examples of acceptors with a TCNE backbone that have been studied. DClNQ forms a glassy ferromagnet when paired with $MnCp^*_2$ (T_c ~ 6 K, θ ~ 3 K) and sparked interest in the prospect of non-cyano-containing acceptors. DCNQ forms an unusual canted metamagnet with $FeCp^*_2$ with a critical field of 3 kG at 1.8 K and T_N ~ 4 K. DCID paired with $FeCp^*_2$ exhibits weak intrastack interactions and does not order above 1.8 K, however, it has proven useful for electron density comparisons with its isomer DCNQ. Finally, MTCE forms magnetic CT salts with all three decamethylmetallocenes and has recently been published.

Chapter III: Dialkyldicyanofumarate Magnets

Dimethyl and diethyl dicyanofumarate (DMeDCF and DEtDCF) have both been studied as organic acceptors for magnetic CT salts.[45, 46] They are structurally and electronically very similar to each other, as well as TCNE. In comparison with TCNE, two of the cyano groups have been replaced by two ester groups, which are also electron-withdrawing (Figure 3.1). The planarity is retained for the most part, however, the size is considerably larger than TCNE. It has been shown that they exhibit reversible one-electron reductions at -0.22 V vs. SCE which is sufficient for reactions with $CrCp^*_2$ and $MnCp^*_2$ but not $FeCp^*_2$ (Figure 3.1). When they were first studied it was thought that DMeDCF and DEtDCF formed CT salts with MCp^*_2 that followed the typical structural motif, each having similar intrastack distances with the length of alkyl groups providing for considerable differences in the interstack distances (2-3 Å). Considering the similarities between these two acceptors, it seemed safe to assume that any differences in the bulk magnetic character of the MCp^*_2 salts could be attributed to the differences in

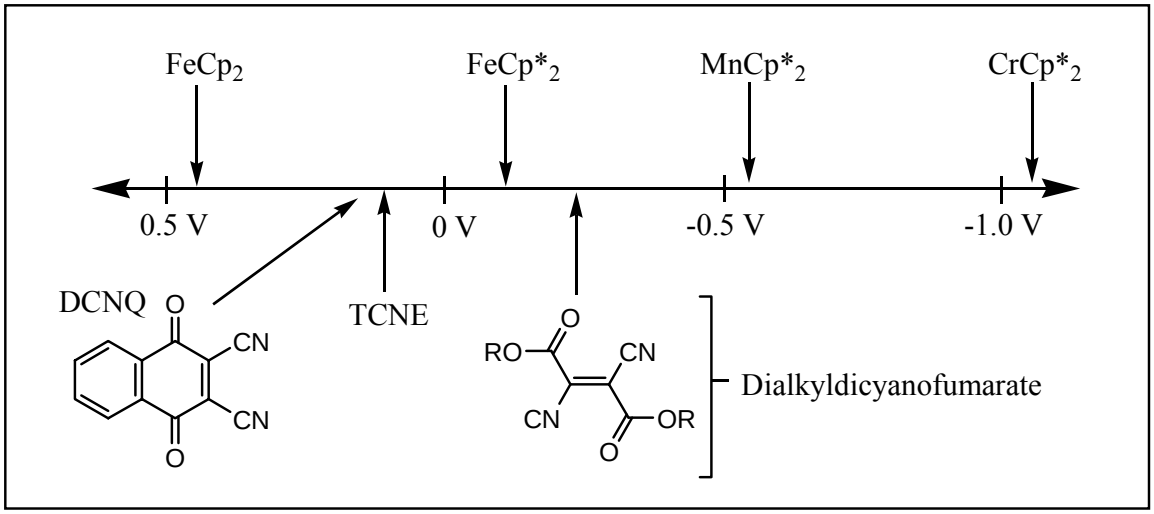

Figure 3.1 Electrochemical properties of a few acceptors and donors. (vs. SCE)

the interstack distances. Recently, however, it was discovered that the decamethylchromocenium salt of the diethyl diester assumed a slightly different stacking pattern than the dimethyl analog which has the typical structure.

In the past, structure-property relationships have proven to be vital in the detailed understanding of magnetic coupling. The idea of synthesizing a family of dialkyldicyanofumarate acceptors where the alkyl group is varied in length offers a convenient method for study structure-property relationships. The key point is that the intrastack distances in the CT salts should remain relatively the same from one acceptor to the next, but the interstack distances will change due to the length of the alkyl group. Research on the dimethyl- and diethyl dicyanofumarates has been previously published and new results from the di-*n*-propyl- and diisopropyl dicyanofumarates will be discussed. Also, current efforts are being made on synthesizing other related dicyanofumarates including alkyl groups with terminal hydroxy groups, as well as the analogous butyl compounds.

1. [MnCp$_2$][DMeDCF]*

The synthesis and magnetic characterization of [MnCp*$_2$][DMeDCF] has been previously reported.[46] Like other MnCp*$_2$ CT salts, it is air sensitive and not stable at room temperature in solution. The structure of this compound was verified by comparison of powder diffraction patterns with those of [CrCp*$_2$][DMeDCF] because of the difficulty in growing crystals for single crystal X-ray crystallography. It was found to be isostructural with the chromium homolog, adopting the $\mathbf{D^+A^-}$ stacking configuration and possessing both in-registry and out-of-registry chains.

The bulk magnetic properties of [MnCp*$_2$][DMeDCF] are similar to the TCNE analog. There is dominant ferromagnetic coupling that gives rise to apparent ferromagnetic ordering below T_c = 10.5 K which is higher than the TCNE analog (T_c = 8.8 K). The plot of χT vs. T shows a sharp peak at approximately 8 K that rises to over 300 emu·G/mol and the plot of χ^{-1} vs. T agrees with the Curie-Weiss law exhibiting θ = +16.0 K. Also, the value of g for MnCp*$_2$ was found to be consistent with previously reported values for other MnCp*$_2$ salts (g = 2.36, assuming g = 2.00 for the organic acceptor). Plots of M vs. H show the evolution of a hard to soft ferromagnet as the temperature is increased with a large coercive field ($H_{cr} \approx$ 7 kG) at 1.8 K. There is some evidence of canting in the ordered state since the saturation magnetization is lower than expected. There is also some evidence that this may not be a true ferromagnet based on significant frequency dependence of the *ac* susceptibility which is indicative of a spin-glass.

2. [MnCp$_2$][DEtDCF]*

The synthesis and magnetic characterization of [MnCp*$_2$][DEtDCF] has been previously reported.[46] Comparisons of powder diffraction patterns with those of the chromium analog, however, were not as useful as with the DMeDCF salt for structural information. The chromium analog has solvent molecules in its crystal structure that would not be present in [MnCp*$_2$][DEtDCF] because of thorough drying due to its instability in solution at room temperature. This suggests that the magnetic data reported for this compound was on a crystallographically disordered solid due to loss of solvent.

The magnetic data for [MnCp*$_2$][DEtDCF] is considerably different from its dimethyl analog. The plot of χT vs. T shows ferromagnetic coupling in one dimension as signified by the sharp rise near 12 K. However, the curve reaches a maximum at about 27 emu·G/mol before decreasing sharply. This is due to the presence of a three dimensional antiferromagnetic phase transition which is also supported by a frequency independent peak in the in-phase component and no out-of-phase component for the *ac* susceptibility. The plot of χ^{-1} vs. T shows good agreement with the Curie-Weiss law with θ = +15.5 K which should be similar to [MnCp*$_2$][DMeDCF] since the intrastack distances are essentially the same. Plots of M vs. H at 9 K are indicative of metamagnetic behavior with the presence of an antiferromagnetic state that switches to a ferromagnetic state upon application of a sufficient critical field ($H_c \approx$ 500 G). At 1.8 K, M vs. H shows hysteresis with a large coercive field ($H_{cr} \approx$ 10 kG) and some asymmetry around the origin which suggests glassiness. This is supported by frequency dependent low temperature *ac* susceptibility and the low temperature separation of the plots of M vs. T for field cooled and zero-field cooled samples.

3. [CrCp$_2$][DMeDCF]*

The synthesis and magnetic characterization of [CrCp*$_2$][DMeDCF] has been previously reported.[45] It is a soft ferromagnet with T_c = 5.7 K which is considerably higher than its TCNE analog (reported independently as T_c = 2.1 K by Hoffman[47] and T_c = 3.65 K by Miller[4]). The crystal structure of [CrCp*$_2$][DMeDCF] exhibits the $\mathbf{D^+A^-}$ stacking pattern with the presence of in-registry and out-of-registry chains (Figure 3.2).

The plot of χT vs. T shows a peak in the curve at approximately 10 K that reaches about 300 emu·K/mol, which is indicative of ferromagnetic coupling. Above 50 K, χ^{-1} vs. T fits the Curie-Weiss law, exhibiting θ = +23 K which is comparable to the results of [CrCp*$_2$][TCNE] (θ = +24 K) from Miller et al.[4] This may suggest that the dominant intrastack interactions are similar in magnitude and sign for both [CrCp*$_2$][DMeDCF] and its TCNE analog. However, as mentioned before, there is some ambiguity in the reported θ values reported for the TCNE analogs that is yet to be understood. Plots of the *ac* susceptibility provides evidence for a ferromagnetic phase transition as illustrated by the peak in χ' at 4.8 K with a non-zero imaginary component. Also, the *ac* susceptibility is nearly frequency-independent, indicating a lack of glassiness. A plot of M vs. H at 1.8 K shows that [CrCp*$_2$][DMeDCF] is a soft ferromagnet with $H_{cr} \approx 50$ G and $M_s \approx 22000$ emu·G/mol which is near the expected value of 22340 emu·G/mol for three unpaired electrons on the donor with g = 2.00 for both donor and acceptor.

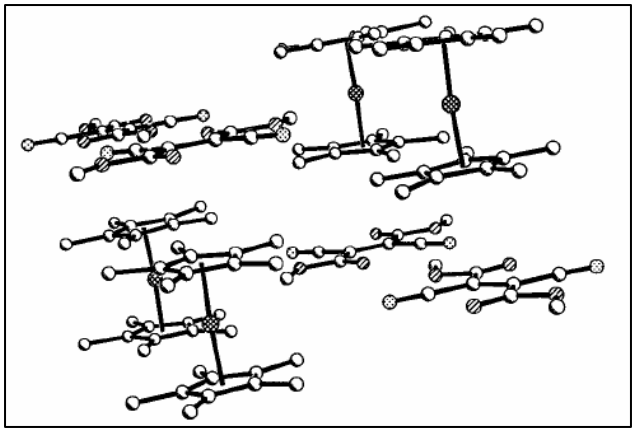

Figure 3.2 Packing diagram for [CrCp*$_2$] [DMeDCF].

4. [CrCp$_2$][DEtDCF]*

The synthesis and magnetic characterization of [CrCp*$_2$][DEtDCF] has been reported.[46] It is a metamagnet with T_N = 5.4 K that shows some similarities to its ferromagnetic dimethyl analog, as well as its metamagnetic manganese analog. The

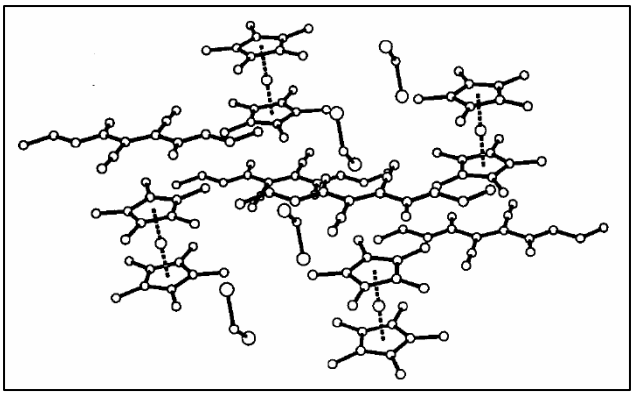

Figure 3.3 Packing diagram for [CrCp*$_2$][DEtDCF] •2CH_2Cl_2.

crystal structure shows the salt to be a dichloromethane solvate, [CrCp*$_2$][DEtDCF]·2CH_2Cl_2 (Figure 3.3). The typical stacking structure is not present, however. The length of the ethyl groups of the diester creates gaps around the CrCp*$_2$ donors which are filled by CH_2Cl_2 molecules. Little is understood about how these solvent molecules affect the interstack interactions between the chromium centers or their role in causing the different stacking pattern.

[CrCp*$_2$][DEtDCF] exhibits θ = +22 K, showing that the dominant intrastack interactions are similar in strength to that of its dimethyl analog. At about 5.4 K, there is the presence of an antiferromagnetic phase transition as indicated by the *ac* susceptibility, which is more reminiscent of its manganese analog. However, based on a plot of field-cooled *M* vs. *T,* the magnetization does not approach zero after the peak at 5.4 K, as expected for an antiferromagnet, but starts to increase again. This may be due to the onset of some type of frustration or glassiness. A plot of *M* vs. *H* at 1.8 K and 5000 G shows the M_s to be only about 70 % of the expected saturation value; the dimethyl analog, however, is fully saturated in these conditions.

5. Dipropyl dicyanofumarates

The magnetic and structural data for the DMeDCF and DEtDCF salts of CrCp*$_2$ and MnCp*$_2$ originally suggested that there may be some correlation between bulk magnetic properties and the interstack distances.[48] However, there are some significant

differences in the structures of the dimethyl and diethyl salts that complicate meaningful comparisons of the two. The first difference is the presence of solvent molecules in the structure of the DEtDCF salt. Secondly, as looking down the stacking axis, the donors and acceptors in the DMeDCF salt form zig-zag chains while in the DEtDCF salt they form linear chains (Figure 3.4). As mentioned before, intrastack distances are essentially the same for both dimethyl and diethyl dicyanofumarate so it is possible that changes in the magnetic properties can be attributed to the interstack distances to some degree. Ferromagnetic interactions within the stacks are dominant when the alkyl group is methyl, however, 3-D antiferromagnetic interactions arise to compete with the intrastack ferromagnetic interactions when the alkyl group is ethyl. Since the interstack distances are dictated by the length of the alkyl group on the dialkyl dicyanofumarate, there is a possible correlation that can be tested by varying the alkyl group and comparing

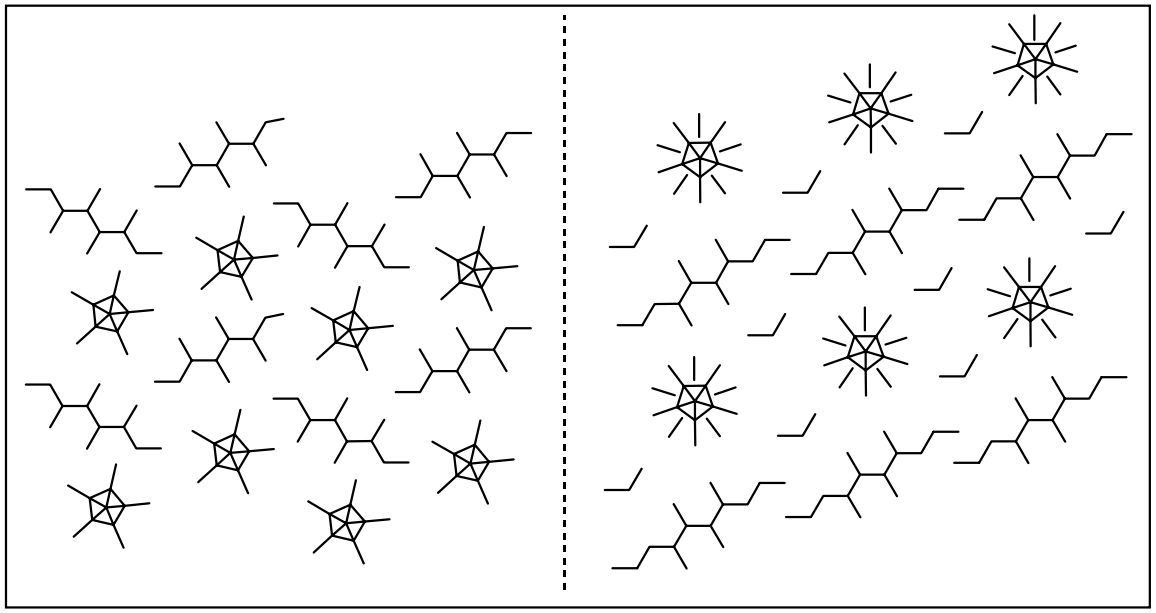

Figure 3.4 View down the stacking axis of (left) [$CrCp^*_2$][DMeDCF] showing zig-zag chains of D^+ and A^- and (right) [$CrCp^*_2$][DEtDCF]•$2CH_2Cl_2$ showing linear chains of D^+ and A^-.

magnetic properties. Two new dicyanofumarate acceptors with longer alkyl groups were introduced: Di-*n*-propyl and di-isopropyl dicyanofumarate (D*n*PrDCF and D*i*PrDCF). These acceptors were found to form CT salts that are structurally more related to the DEtDCF salt. Therefore, when comparing magnetic properties, any changes can be attributed to the bulkiness of the alkyl group of the diester.

6. Experimental Section

6.1. General Considerations

Preparations of air-sensitive compounds were carried out in a nitrogen-filled Vacuum Atmospheres glove box maintained at less than 5 ppm O_2 and by utilizing standard Schlenk techniques. Decamethylchromocene and decamethylmanganocene were purchased from Strem Chemicals. All other reagents were purchased from Aldrich. Reagents were used as purchased except as noted below. Methylene chloride was distilled from P_2O_5. Diethyl ether was distilled from Na/benzophenone. All solvents were degassed with glove box N_2 prior to use. Di-*n*-propyl dicyanofumarate and di-isopropyl dicyanofumarate were synthesized by a previously published route.[49] Elemental analyses were performed by Desert Analytics, Tucson, AZ.

6.2. Magnetic Measurements

All the magnetic measurements were performed on a 7 T Quantum Design MPMS SQUID magnetometer. Measurements of magnetization as a function of temperature were performed from 1.8 K to 300 K and in a 1000 G field. Powder samples were cooled in zero applied field and measured upon warming. Samples were prepared as previously

described.[50] The amplitude of the oscillating magnetic field used for *ac* susceptibility measurements was 3.5 Oe with zero *dc* bias field and at frequencies of 1, 10, 100, and 1000 Hz. Diamagnetic corrections were applied based on Pascal's constants for χT plots but no corrections were applied for M vs. H or ac data.

6.3. X-ray Crystallography

Dark Red plates (0.12 x 0.12 x 0.055 mm^3) of decamethylchromocenium di-isopropyl dicyanofumarate, [Cr(Cp*)$_2$][D*i*PrDCF]**,** were crystallized from dichloromethane by slow diffusion of pentane at room temperature in the glovebox. The chosen crystal was mounted on a nylon CryoLoop™ (Hampton Research) with Krytox® Oil (DuPont) and centered on the goniometer of an Oxford Diffraction Xcalibur2™ diffractometer equipped with a Sapphire 2™ CCD detector. The data collection routine, unit cell refinement, and data processing were carried out with the program CrysAlis.[51] The Laue symmetry was consistent with the triclinic space group *P*-1. The structure was solved by direct methods using Sir92[52] via the WinGX[53] graphical user interface. The structure was refined using the SHELXTL NT program package.[54] The asymmetric unit of the structure comprises 0.5 crystallographically independent [CrCp*$_2$][D*i*PrDCF] formula unit and one CH_2Cl_2 solvate. The final refinement model involved anisotropic displacement parameters for non-hydrogen atoms and a riding model for all hydrogen atoms. The program package SHELXTL NT was used for molecular graphics generation.[54]

6.4. Decamethylchromocenium Di-n-propyl Dicyanofumarate, [CrCp$_2$][DnPrDCF]*

Decamethylchromocene (55 mg, 1.7×10^{-4} mol) was dissolved in 2 ml of CH_2Cl_2. To this solution was added a solution of di-*n*-propyl dicyanofumarate (40 mg, 1.6×10^{-4} mol) in 2 ml of CH_2Cl_2. Immediately, the color of the solution turned from yellow to brown. After the solution had stirred for 0.5 hours at room temperature, 12 ml of diethyl ether was slowly added to precipitate an air-sensitive, brown solid. This solid was filtered, washed with diethyl ether, and dried in vacuo. Yield: 43.6 mg (47.7 %). Anal. Calcd for [$CrCp^*_2$][D*n*PrDCF] · CH_2Cl_2, $C_{33}H_{46}N_2O_4Cl_2Cr$: C, 60.27; H, 7.05; N, 4.26. Found: C, 59.46; H, 7.31; N, 4.23.

6.5 Decamethylchromocenium Di-isopropyl Dicyanofumarate, [$CrCp^*_2$][DiPrDCF]

This salt was synthesized using the same procedure stated immediately above. Yield: 26.8 mg (29.0 %) Anal. Calcd for [$CrCp^*_2$][D*i*PrDCF] · CH_2Cl_2, $C_{33}H_{46}N_2O_4Cl_2Cr$: C, 60.27; H, 7.05; N, 4.26. Found: C, 59.82; H, 7.42; N, 4.41.

6.6 Decamethylmanganocenium Di-n-propyl Dicyanofumarate, [$MnCp^*_2$][DnPrDCF]

Decamethylmanganocene (51 mg, 1.6×10^{-4} mol) was dissolved in 2 ml of CH_2Cl_2, and the solution was cooled to -77 °C using a dry ice/acetone bath. To this solution was added a solution of di-*n*-propyl dicyanofumarate (37 mg, 1.5×10^{-4} mol) in 3 ml CH_2Cl_2. The solution turned from yellow to brown after addition of a few drops. After the solution had stirred for 0.5 hours at -77 °C, 12 ml of diethyl ether was slowly added to precipitate a greenish brown solid. This solid was collected on a pre-cooled glass frit and washed with diethyl ether. The solid was dried in vacuo at low temperature for 2 hours, then 0.5 hours at room temperature. Yield: 72.2 mg (87.8 %) Anal. Calcd

for [MnCp*$_2$][D*n*PrDCF] · 0.05CH_2Cl_2, $C_{32.05}H_{44.1}N_2O_4Cl_{0.1}Mn$: C, 66.38; H, 7.66; N, 4.83. Found: C, 65.72; H, 7.92; N, 4.83.

6.7 Decamethylmanganocenium Di-isopropyl Dicyanofumarate, [MnCp$_2$][DiPrDCF]*

This salt was synthesized using the same procedure stated immediately above. Yield: 64.6 mg (78.6 %) Anal. Calcd for partially solvated [MnCp*$_2$][D*i*PrDCF] · 0.5CH_2Cl_2, $C_{32.05}H_{44.1}N_2O_4Cl_{0.1}Mn$: C, 66.38; H, 7.66; N, 4.83. Found: C, 66.85; H, 7.45; N, 4.71.

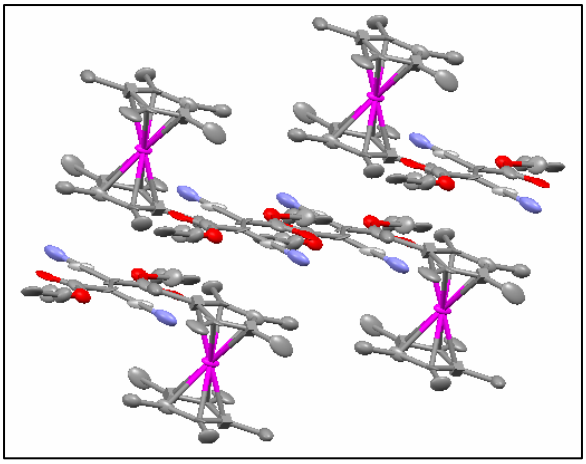

Figure 3.5 Packing diagram for [CrCp*$_2$] [D*n*PrDCF]

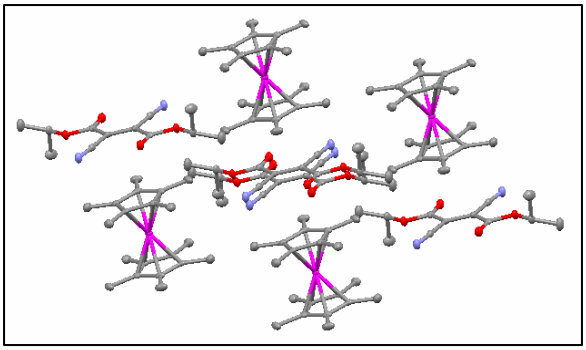

Figure 3.6 Packing diagram for [CrCp*$_2$] [D*i*PrDCF]

7. Discussion

7.1. Structure

The crystal structures of [CrCp*$_2$][D*n*PrDCF] (Figure 3.5) and [CrCp*$_2$][D*i*PrDCF] (Figure 3.6) have been solved and display similar structures to the diethyl analog. The structure of the di-isopropyl analog was solved as described above. The di-*n*-propyl analog did not crystallize very well, however, a low resolution structure solution describing symmetry and unit cell parameters was obtained. Each of them has two solvent molecules per formula

Table 3.1 Unit cell information for each salt of the homologous series.

Salt	[CrCp*$_2$][DMeDCF]	[CrCp*$_2$][DEtDCF]•2CH_2Cl_2	[CrCp*$_2$][D*n*PrDCF]•2CH_2Cl_2	[CrCp*$_2$][D*i*PrDCF]•2CH_2Cl_2
Formula	$C_{28}H_{36}CrN_2O_4$	$C_{32}H_{44}Cl_4CrN_2O_4$	$C_{34}H_{48}Cl_4CrN_2O_4$	$C_{34}H_{48}Cl_4CrN_2O_4$
MW	516.60	714.52	742.57	742.57
Space Group	P*nma*	P-1	P-1	P-1
a (Å)	16.0414	9.6239	9.4294	9.7212
b (Å)	10.6907	9.6880	9.8001	9.7292
c (Å)	15.6571	11.1488	11.5918	11.5723
α (°)	90	81.36	78.15	80.76
β (°)	90	69.09	71.23	68.78
γ (°)	90	66.02	65.97	66.33
V (Å^3)	2685.10	887.23	922.96	934.33
Z	4	1	1	1

unit as well as having the same alternating $\mathbf{D^+A^-}$ stacking motif. A considerable difference is the sterics of the di-isopropyl analog as compared to DEtDCF and D*n*PrDCF which are planar. This increases the intrastack distance slightly, but they are essentially the same for all of these compounds, including the dimethyl analog. A table for structure comparison of each salt of the homologous series is included. (Table 3.1)

There are some significant differences in the structures of the dimethyl analog and the other salts that should be considered. An obvious difference is that the dimethyl analog is not a solvate while the other salts are dichloromethane solvates. Also, there some specific differences in the $\mathbf{D^+A^-}$ intrastack arrangements. The metallocene of the dimethyl analog is centered over the inversion center of the acceptor within the stacks forming a straight stack while there is a slight offset in the other salts which forms a stepped structure with the di-isopropyl analog offset being slightly larger than the diethyl or di-*n*-propyl. Also, the methyls on each decamethylchromocene of the dimethyl analog are eclipsed while the other salts display a staggered conformation. A key difference can be observed when looking down the stacking axis of the structures. The donors in the

Table 3.2 Cr-Cr separation in each salt of the homologous series.

Salt	[$CrCp^*_2$] [DMeDCF]	[$CrCp^*_2$] [DEtDCF]	[$CrCp^*_2$] [D*n*PrDCF]	[$CrCp^*_2$] [D*i*PrDCF]
intrastack (Å)	10.691	10.521	10.474	10.641
interstack in-registry (Å)	9.103	9.624	9.429	9.721
Nearest out-of-registry (Å)	9.545	11.149	11.592	11.572
next-nearest out-of registry (Å)	11.156	11.846	12.367	12.124

dimethyl analog form a zig-zag chain while in the other salts they form a straight chain (Figure 3.4). The zig-zag pattern allows for a significant decrease in interstack distances (Table 3.2).

As previously mentioned, crystal structures of the $MnCp^*_2$ salts have not been obtained due to the difficulty in growing single crystals of them. It is possible to get some structural information from the comparison of powder diffraction patterns of $MnCp^*_2$ salts with their $CrCp^*_2$ analogs, but recent attempts at getting useful powder diffraction patterns for this purpose have been unsuccessful. It is a reasonable assumption, however, to assume that the $MnCp^*_2$ salts of D*i*PrDCF and D*n*PrDCF are structurally similar to their $CrCp^*_2$ analogs.

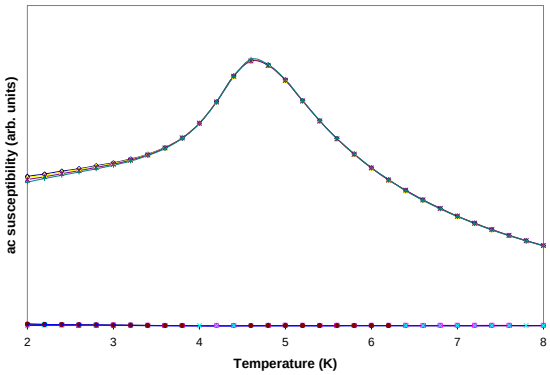

Figure 3.7 *ac* susceptibility of [$CrCp^*_2$] [D*n*PrDCF]

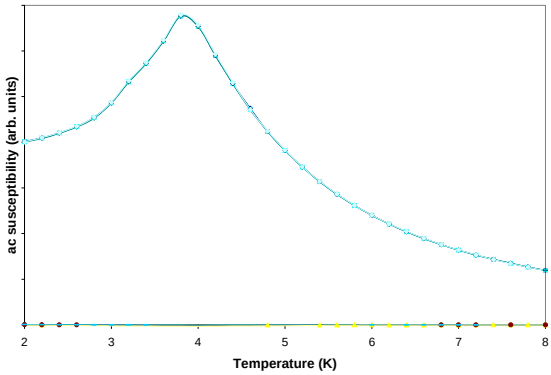

Figure 3.8 *ac* susceptibility of [$CrCp^*_2$] [D*i*PrDCF]

7.2. Magnetic Properties of CrCp$_2$ Salts*

Magnetic data collected for samples of [CrCp*$_2$][D*n*PrDCF] and [CrCp*$_2$][D*i*PrDCF] indicates that they are metamagnets. This is supported by plots of the *ac* susceptibility for each salt which show frequency independent peaks in χ' at 4.6 and 3.9 K, respectively, with no χ'' component (Figures 3.7 and 3.8). Further evidence is provided by the *M* vs. *H* plots in which each displays the characteristic sigmoidal shape around the origin (Figures 3.9 and 3.10). Along with the diethyl analog which exhibits T_N = 5.4 K, a weak trend exists in ordering temperature and the bulkiness of the diester's alkyl group supporting an earlier hypothesis concerning bulk character and interstack distances. The dimethyl analog also follows this trend ordering at T_c = 5.7 K and having the least bulky alkyl group on the diester as well as the shortest interstack distances. However, [CrCp*$_2$][TCNE] doesn't fit in since it orders lower than any species in this series, T_c = 2.1 K while containing the least bulky acceptor. It may be coincidence that the dimethyl analog follows the aforementioned trend since it and [CrCp*$_2$][TCNE] are actually more closely related to each other than the homologous series. Both are ferromagnets having the zig-zag chains of $\mathbf{D}^+$ and $\mathbf{A}^-$ as illustrated in figure 3.4 and both have no solvent molecules in their crystal structures.

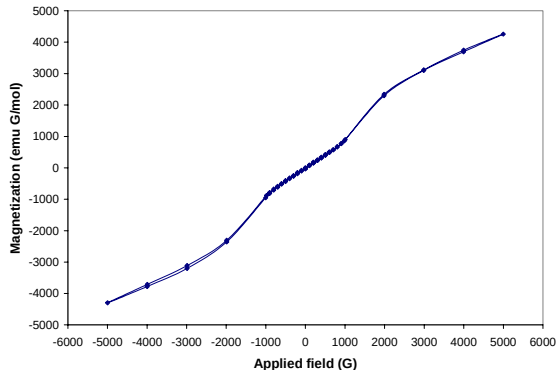

Figure 3.9 *M* vs. *H* plot for [CrCp*$_2$][D*n*PrDCF]

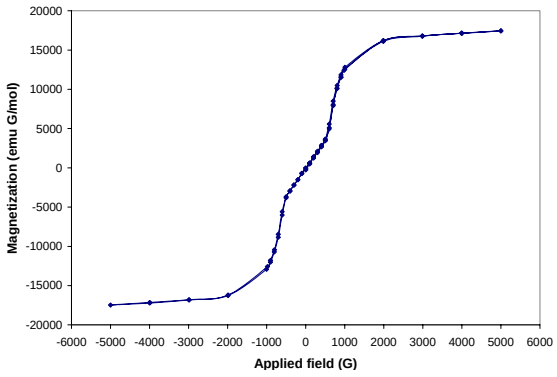

Figure 3.10 *M* vs. *H* plot for [CrCp*$_2$][D*i*PrDCF]

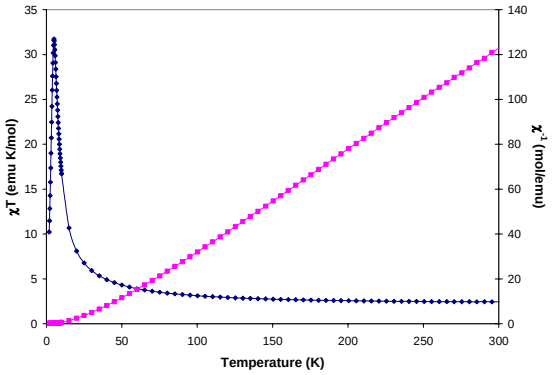

Figure 3.11 χT and χ^{-1} vs. T for [CrCp*$_2$][D*n*PrDCF]

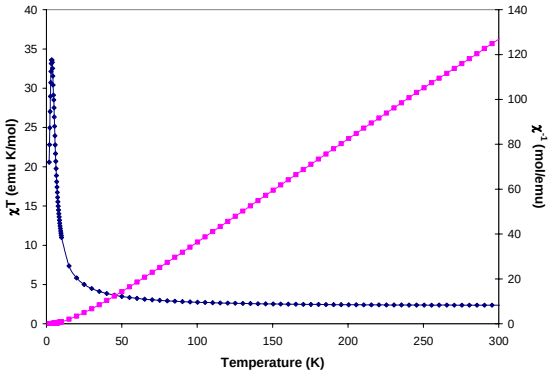

Figure 3.12 χT and χ^{-1} vs. T for [CrCp*$_2$][D*i*PrDCF]

The plots of χT vs. T and χ^{-1} vs. T for [CrCp*$_2$][D*n*PrDCF] and [CrCp*$_2$][D*i*PrDCF] are shown in figures 3.11 and 3.12. The plots exhibit a dramatic rise in χT as the temperature is lowered. It rises from 2.44 emu K/mol at 300 K to approximately 32 emu K/mol at 5.0 K for the di-*n*-propyl analog and 2.36 emu K/mol at 300 K to approximately 33 emu K/mol at 3.4 K for the di-isopropyl analog. Above 50 K the data for both salts follows the Curie-Weiss law, giving C = 2.19 emu K/mol and θ = 30 K for [CrCp*$_2$][D*n*PrDCF] and C = 2.20 emu K/mol and θ = 19 K for [CrCp*$_2$][D*i*PrDCF]. Both values of the Curie constant are close to the expected value of C = 2.25 emu K/mol and the θ values reflect the dominant intrastack ferromagnetic interactions. The di-*n*-propyl analog has a higher θ indicating stronger ferromagnetic interactions which agrees with its shorter intrastack distances. The diethyl analog has θ = 22 K which falls between each of the above θ values. This is also in agreement since the intrastack distance for the diethyl analog is between that of the di-*n*-propyl and di-isopropyl analogs. However, the dimethyl analog exhibits θ = 23 K and has the largest intrastack distance of the homologous series. This does not agree with the proposed trend

but may be attributed to different types of interactions due to the differences in structure previously discussed.

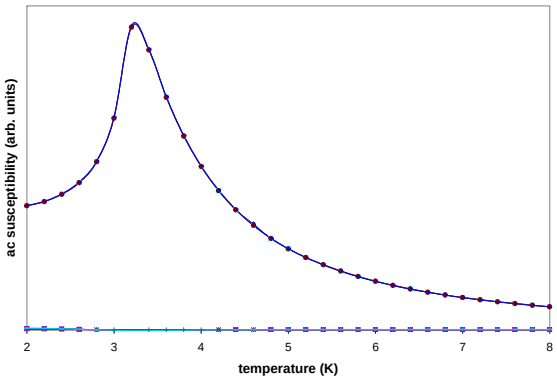

Figure 3.13 *ac* susceptibility of [CrCp*$_2$][D*i*PrDCF] in excess solvent

The elemental analyses for [CrCp*$_2$][D*n*PrDCF] and [CrCp*$_2$][D*i*PrDCF] suggested that there was one solvent molecule of methylene chloride for each formula unit, however, single crystal x-ray crystallography revealed two solvent molecules per formula unit. There was some concern that these samples were losing solvent when placed under vacuum for sealing glass sample containers. The *ac* susceptibility data for the di-isopropyl analog shows some slight frequency dependence at temperatures below the T_N, indicating the onset of spin frustration. Since the measurement was made on a sample that had been place under vacuum for some amount of time, it is reasonable to assume that this frustration arises from disorder in the structure due to loss of solvent. This hypothesis was confirmed by performing the same measurement on a sample in excess solvent. Figure 3.13 shows the *ac* susceptibility data for a sample of the di-isopropyl analog which displays a sharper peak and no apparent onset of frustration. More importantly, there is no apparent change in T_N which indicates that magnetic measurements performed on slightly desolvated samples are representative of the proposed structure.

Another weak trend exists in θ values and intrastack distances. Plots of χ^{-1} vs. T for [CrCp*$_2$][D*n*PrDCF] and [CrCp*$_2$][D*i*PrDCF] show that $\theta \approx 30$ K and 19 K respectively. It is possible to arrange the homologous series in order of increasing

intrastack distances (Table 3.3). The di-*n*-propyl analog has the shortest distance and accordingly has the highest θ of the series. The dimethyl analog should have the smallest θ of the series, however, its deviation could be explained by a lesser antiferromagnetic contribution from the interstack distances. This is reasonable since its stacking pattern is significantly different from the others. Also, it has been suggested that interstack interactions may be a complex mixture of the effects of several mechanisms which bring about a competition between ferromagnetic and antiferromagnetic coupling.

Table 3.3 Comparison of intrastack distances and θ values

Salt	Intrastack Distance (Å)	θ (K)
[CrCp*$_2$][D*n*PrDCF]	10.474	30
[CrCp*$_2$][DEtDCF]	10.521	22
[CrCp*$_2$][D*i*PrDCF]	10.641	19
[CrCp*$_2$][DMeDCF]	10.691	23

7.3. Magnetic Properties of MnCp$_2$ Salts*

Structural parameters for [MnCp*$_2$][D*n*PrDCF] and [MnCp*$_2$][D*i*PrDCF] are not available due to the inability to obtain single crystals or powder diffraction data.

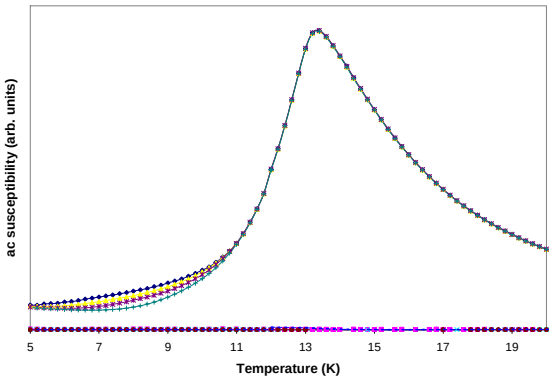

Figure 3.14 *ac* susceptibility for [MnCp*$_2$][D*n*PrDCF]

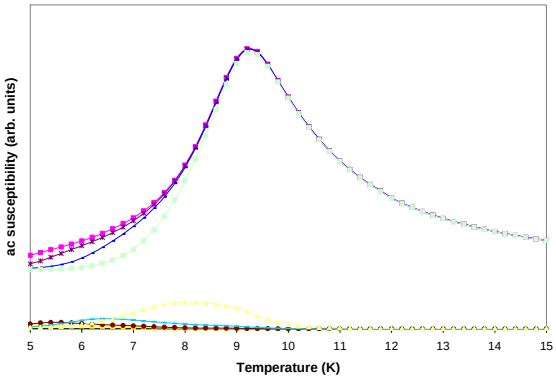

Figure 3.15 *ac* susceptibility for [MnCp*$_2$][D*i*PrDCF]

However, as stated before, it is reasonable to assume these salts are structurally related to their analogous $CrCp^*_2$ salts. Magnetic data suggests that both are metamagnets with T_N= 13.4 K and 9.3 K, respectively. This is supported by *ac* susceptibility data (Figures 3.14 and 3.15) as well as plots of *M* vs. *H* at temperatures just below each respective T_N (Figure 3.16).

The *ac* susceptibility data illustrates peaks in reference to the T_N, which refer to the presence of antiferromagnetic phase transitions, as well as the onset of a glassy magnetic state at lower temperatures. This glassiness may be due to frustration arising from disorder in the structures from desolvation during preparation. As indicated by elemental analysis, both salts appear to be completely desolvated which would create some deviation from the defined structure of the chromium analogs. However, both salts exhibit reproducible magnetic data (*ac* and *M* vs. *H*) which is similar to that of the diethyl

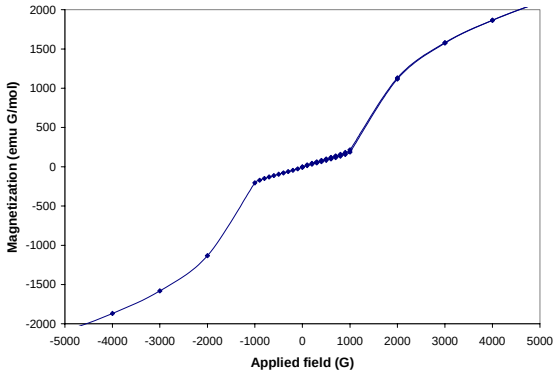

Figure 3.16 *M* vs. *H* plot for [MnCp*$_2$] [D*n*PrDCF] at 9 K.

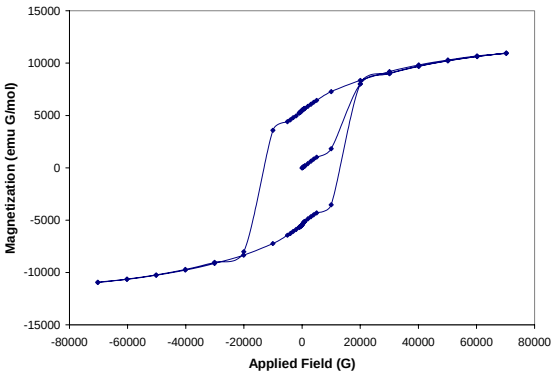

Figure 3.17 *M* vs. *H* plot for [MnCp*$_2$] [D*n*PrDCF] at 1.8 K.

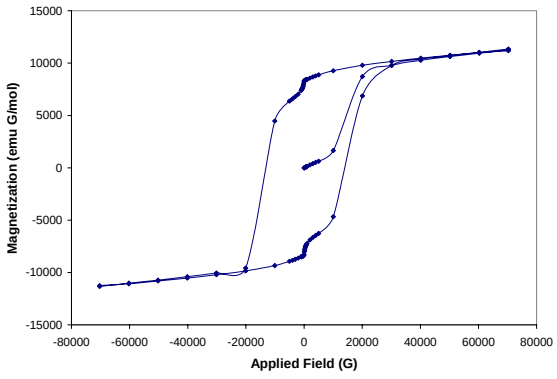

Figure 3.18 *M* vs. *H* plot for [MnCp*$_2$] [D*i*PrDCF] at 1.8 K.

analog. Plots of M vs. H just below T_N of each salt have the characteristic sigmoidal shape of metamagnets. As the temperature is lowered into the glassy range, however, a wide hysteresis loop opens up. At 1.8 K, the di-*n*-propyl analog exhibits a coercive field of 1.3 T with a remanence of 5500 G and the diisopropyl analog exhibits the same coercive field with a remanence of 8000 G (Figures 3.17 and 3.18).

Plots of χT vs. T for [MnCp*$_2$][D*n*PrDCF] and [MnCp*$_2$][D*i*PrDCF] are representative of dominant ferromagnetic coupling (Figures 3.19 and 3.20). The di-*n*-propyl analog exhibits χT of 1.54 emu K/mol at 300 K which rises to a maximum of 16 emu K/mol at about 15 K with C = 1.39 emu K/mol. The diisopropyl analog exhibits χT of 2.04 emu K/mol at 300 K which rises to a maximum of 35 emu K/mol at 8.4 K with C = 1.99 emu K/mol. Plots of χ^{-1} vs. T allowed for estimated θ values of 24 K and 5.5 K, respectively. The θ value of the di-*n*-propyl analog was higher than expected, as compared to the other salts, however, a lack of structural information prevents any true comparison of θ values.

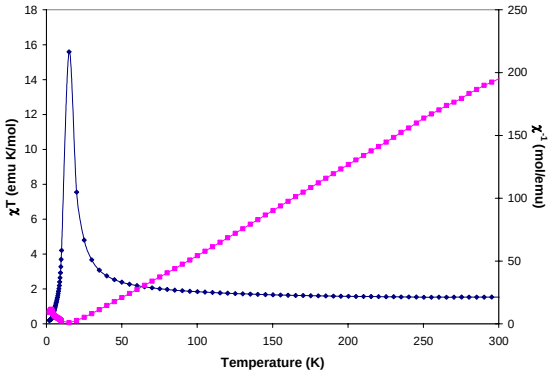

Figure 3.19 χT and χ^{-1} vs. T plot for [MnCp*$_2$][D*n*PrDCF]

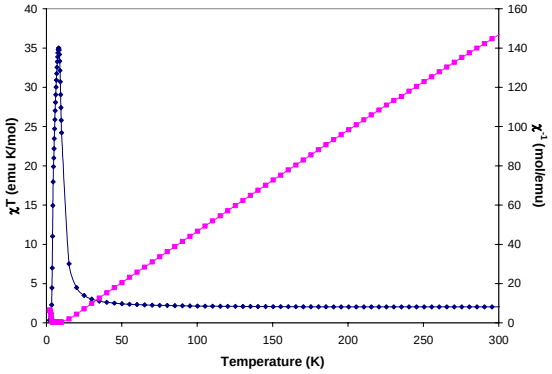

Figure 3.20 χT and χ^{-1} vs. T plot for [MnCp*$_2$][D*i*PrDCF]

In general, the magnetic data for MnCp*$_2$][D*n*PrDCF] and [MnCp*$_2$][D*i*PrDCF] compares nicely with the

diethyl analog. There is some variation in the χT vs. T data resulting in differing values of χT near room temperature, Curie constants, and g values. Data for the di-*n*-propyl analog suggests $g = 2.02$, which is significantly lower than the expected 2.4 (data for the diisopropyl analog suggests $g = 2.54$). Some insight into this difference may be gained by structural information. As stated earlier, it may be possible to get sufficient powder diffraction data in the future on a more crystalline powder sample. However, there is an apparent trend in the ordering temperatures for the homologous series, excluding the diisopropyl analog (Table 3.4).

Table 3.4 Trend in ordering temperature and length of alkyl group.

Salt	Ordering Temp.
[MnCp*$_2$][DMeDCF]	T_c = 10 K
[MnCp*$_2$][DEtDCF]	T_N = 12 K
[MnCp*$_2$][D*i*PrDCF]	T_N = 13.4 K

7.4. Conclusions

Thus far, the dialkyldicyanofumarate family of one-electron organic acceptors for the synthesis of CT salt magnets has proven useful for establishing some weak trends in structure-property relationships. These include ordering temperature and bulkiness of the alkyl group, as well as θ values and intrastack distances. These weak trends tentatively reinforce the previous notion concerning the effects of intra- and interstack distances on the magnetic properties. General magnetic properties of the CrCp*$_2$ and MnCp*$_2$ salts of this family of acceptors are listed in table 3.5. Studies on the analogous butyl compounds should provide more information concerning the validity of these trends.

Also, the unusual stacking pattern displayed by the diethyl- and dipropyldicyanofumarate salts had not been observed until close examination and comparison of the crystal structures for each salt in the family. The differences of

stacking between the DMeDCF salt and the others raises more questions about the role of the solvent molecule in the structure, as well as how it affects the magnetic properties. In attempt to probe this issue, related acceptors are being prepared with terminal hydroxy groups on the alkyl groups which may interact with solvent molecules through hydrogen bonding. This could possibly help to prevent desolvation during SQUID sample preparation as well as reduce disorder due to solvent in the crystal. Also, further efforts to prepare more crystalline $MnCp^*_2$ salts for powder diffraction will provide firmer evidence for structural relationships with the chromium analogs.

Table 3.5 General magnetic properties of dialkyldicyanofumarate salts of $CrCp^*_2$ and $MnCp^*_2$

$[CrCp^*_2][DMeDCF]$	Ferromagnet	T_c=5.7 K	$[MnCp^*_2][DMeDCF]$	Ferromagnet	T_c=10 K
$[CrCp^*_2][DEtDCF]$	Metamagnet	T_N=5.4 K	$[MnCp^*_2][DEtDCF]$	Metamagnet	T_N=12 K
$[CrCp^*_2][D\textit{n}PrDCF]$	Metamagnet	T_N=4.6 K	$[MnCp^*_2][D\textit{n}PrDCF]$	Metamagnet	T_N=13.4 K
$[CrCp^*_2][D\textit{i}PrDCF]$	Metamagnet	T_N=3.9 K	$[MnCp^*_2][D\textit{i}PrDCF]$	Metamagnet	T_N=9.3 K

Bibliography

[1] G. T. Yee, M. J. Whitton, R. D. Sommer, C. M. Frommen, W. M. Reiff, *Inorg. Chem.* **2000**, *39*, 1874.

[2] J. S. Miller, J. C. Calabrese, H. Rommelmann, S. R. Chittipeddi, J. H. Zhang, W. M. Reiff, A. J. Epstein, *J. Am. Chem. Soc.* **1987**, *109*, 769.

[3] G. T. Yee, J. M. Manriquez, D. A. Dixon, R. S. McLean, D. M. Groski, R. B. Flippen, K. S. Narayan, A. J. Epstein, J. S. Miller, *Adv. Mater.* **1991**, *3*, 309.

[4] J. S. Miller, R. S. McLean, C. Vazquez, J. C. Calabrese, F. Zuo, A. J. Epstein, *J. Mater. Chem.* **1993**, *3*, 215.

[5] J. B. Goodenough, *Phys. Rev.* **1955**, *100*, 564.

[6] J. Kanamori, *J. Phys. Chem. Solids* **1959**, *10*, 87.

[7] P. W. Anderson, *Sol. State Phys.* **1963**, *14*, 99.

[8] A. N. Holden, B. T. Matthias, P. W. Anderson, H. W. Lewis, *Phys. Rev.* **1956**, *102*, 1463.

[9] R. M. Bozorth, H. J. Williams, D. E. Walsh, *Phys. Rev.* **1956**, *103*, 572.

[10] S. Ferlay, T. Mallah, R. Ouahes, P. Veillet, M. A. Verdaguer, *Nature* **1995**, *378*, 701.

[11] J. S. Miller, J. L. Manson, *Acc. Chem. Res.* **2001**, *34*, 563.

[12] H. H. Wickman, A. M. Trozzolo, H. J. Williams, G. W. Hull, F. R. Merritt, *Phys. Rev.* **1967**, *155*, 563.

[13] C. G. Barraclough, R. L. Martin, S. Mitra, *J. Chem. Phys.* **1970**, *53*, 1638.

[14] L. J. d. Jongh, A. R. Miedema, *Adv. Phys.* **1974**, *24*, 1.

[15] C. Bellitto, P. Day, *J. Mater. Chem.* **1992**, *2*, 265.

[16] J. M. Manriquez, G. T. Yee, R. S. McLean, A. J. Epstein, J. S. Miller, *Science* **1991**, *252*, 1415.

[17] E. B. Vickers, I. D. Giles, J. S. Miller, *Chem. Mater.* **2005**, *17*, 1667.

[18] E. B. Vickers, T. D. Selby, M. S. Thorum, M. L. Tailiaferro, J. S. Miller, *Inorg. Chem.* **2004**, *43*, 6414.

[19] K. I. Pokhodnya, E. B. Vickers, M. Bonner, A. J. Epstein, J. S. Miller, *Chem. Mater.* **2004**, *16*, 3218.

[20] O. Kahn, Y. Pei, M. Verdaguer, J. P. Renard, J. Sletten, *J. Am. Chem. Soc.* **1988**, *110*, 782.

[21] J. F. Letard, P. Guionneau, L. Rabardel, J. A. K. Howard, A. E. Goeta, D. Chasseau, O. Kahn, *Inorg. Chem.* **1998**, *37*, 4432.

[22] J. F. Letard, J. A. Real, N. Moliner, A. B. Gaspar, L. Capes, O. Cador, O. Kahn, *J. Am. Chem. Soc.* **1999**, *121*, 10630.

[23] O. Cador, C. Mathoniere, O. Kahn, *Inorg. Chem.* **2000**, *39*, 3799.

[24] V. H. Crawford, H. W. Richardson, J. R. Wasson, D. J. Hodgson, W. E. Hatfield, *Inorg. Chem.* **1976**, *15*, 2107.

[25] P. J. Hay, J. C. Thibeault, R. Hoffmann, *J. Am. Chem. Soc.* **1976**, *97*, 4884.

[26] W. E. Marsh, T. L. Bowman, C. S. Harris, W. E. Hatfield, D. J. Hodgson, *Inorg. Chem.* **1981**, *20*, 3864.

[27] W. E. Hatfield, J. J. MacDougall, R. E. Shepherd, *Inorg. Chem.* **1981**, *20*, 3864.

[28] M. Wei, R. D. Willett, *Inorg. Chem.* **1996**, *35*, 6381.

[29] M. Wei, R. D. Willett, *Inorg. Chem.* **1996**, *35*, 5781.
[30] G. S. Long, M. Wei, R. D. Willett, *Inorg. Chem.* **1997**, *36*, 3102.
[31] R. D. Willett, C. Galeriu, C. P. Landee, M. M. Turnbull, B. Twamley, *Inorg. Chem.* **2004**, *43*.
[32] A. Figuerola, C. Diaz, J. Ribas, V. Tangoulis, C. Sangregorio, D. Gatteschi, M. Maestro, J. Mahia, *Inorg. Chem.* **2003**, *42*, 5274.
[33] A. Caneschi, D. Gatteschi, P. Rey, R. Sessoli, *Chem. Mater.* **1992**, *4*, 204.
[34] R. Sessoli, H. L. Tsai, A. R. Schake, S. Wang, J. B. Vincent, K. Folting, D. Gatteschi, G. Christou, D. N. Hendrickson, *J. Am. Chem. Soc.* **1993**, *115*, 1804.
[35] D. Gatteschi, O. Guillou, C. Zanchini, R. Sessoli, O. Kahn, M. Verdaguer, Y. Pei, *Inorg. Chem.* **1989**, *28*, 287.
[36] J. M. Herrera, A. Bleuzen, Y. Dromzee, M. Julve, F. Lloret, M. Verdaguer, *Inorg. Chem.* **2003**, *42*, 7052.
[37] F. Pointillart, C. Train, M. Gruselle, F. Villain, H. W. Schmalle, D. Talbot, P. Gredin, S. Decurtins, M. Verdaguer, *Chem. Mater.* **2004**, *16*, 832.
[38] D. Gatteschi, *The Coordination Chemistry of Metalloenzymes*, I ed., D. Reidel, Dordrecht, Holland, **1982**.
[39] H. M. McConnell, *Proc. Robert A. Welch Found. Conf. Chem. Res.* **1967**, *11*, 144.
[40] J. S. Miller, A. J. Epstein, *Angew. Chem. Int. Ed. Engl.* **1994**, *33*, 385.
[41] C. Kollmar, O. Kahn, *Acc. Chem. Res.* **1993**, *26*, 259.
[42] H. M. McConnell, *J. Chem. Phys.* **1963**, *39*.
[43] M. Deumal, J. J. Novoa, M. J. Bearpark, P. Celani, M. Olivucci, M. A. Robb, *J. Phys. Chem. A* **1998**, *102*, 8404.
[44] G. Wang, C. Slebodnick, R. J. Butcher, M. C. Tam, T. D. Crawford, G. T. Yee, *J. Am. Chem. Soc.* **2004**, *126*, 16890.
[45] B. B. Kaul, R. D. Sommer, B. C. Noll, G. T. Yee, *Inorg. Chem.* **2000**, *39*, 865.
[46] B. B. Kaul, W. S. Durfee, G. T. Yee, *J. Am. Chem. Soc.* **1999**, *121*, 6862.
[47] D. M. Eichhorn, D. C. Skee, W. E. Broderick, B. M. Hoffman, *Inorg. Chem.* **1993**, *32*, 491.
[48] B. B. Kaul, B. C. Noll, G. T. Yee, *J. Solid State Chem.* **2001**, *159*, 420.
[49] C. J. Ireland, K. Jones, J. S. Pizey, S. Johnson, *Synth. Commun.* **1976**, *3*, 185.
[50] S. P. Sellers, B. J. Korte, J. P. Fitzgerald, W. M. Reiff, G. T. Yee, *J. Am. Chem. Soc.* **1998**, *120*, 4662.
[51] Oxford Diffraction, Wroclaw, Poland, **2004**.
[52] A. Altomare, G. Cascarano, C. Giacovazzo, A. Guagliardi, *J. Appl. Cryst.* **1993**, *26*, 343.
[53] L. J. Farrugia, *J. Appl. Cryst.* **1999**, *32*, 837.
[54] G. M. Sheldrick, Bruker Analytical X-ray Systems, Inc., Madison, WI, **2001**.